



University  
of Stavanger

Faculty of Science and Technology

## MASTER'S THESIS

Study program/Specialization: <b>Offshore Technology/Marine and Subsea Technology</b>	Spring semester, 2023 <b>Open/<del>Restricted access</del></b>
Writer: <b>Osasenaga Igbinomwanhia</b>	..... (Writer's signature)
Faculty Supervisor: <b>Dr. Charlotte Obhrai</b> External Supervisor(s):	
Thesis title: <b>Study to Determine which Turbulence Models are Best Suitable for Offshore Environment in Non-Neutral Conditions</b>	
Credit (ECTS): <b>30</b>	
Keywords:	<b>Pages: 78</b> <b>+ enclosure: 1CD</b> <b>Stavanger,</b>

**Abstract:**

Wind turbines have been experiencing a rapid development over the years and there has been a shift from onshore to offshore. The lateral and vertical coherences at various locations on the floating wind turbine rotor were thought to have an impact on the floater motions due to their spatial connection. It has been hypothesized that the wind turbine components will suffer substantial fatigue damage unlike most offshore structures which are more affected by ultimate limits states because of the unstable air stability conditions that more frequently occur offshore. This work investigated the impact of turbulence on the on the performance of offshore wind farms, as well as the unique qualities of offshore wind turbines. While taking analysis of atmospheric stability and various turbulence spectral models, we were able to ascertain the one that is most suitable for offshore environment in a non-neutral condition. In this research it was observed that the peak value for the non-dimensional velocity spectra was larger for the neutral stability conditions (with the maximum value reaching unity), followed by the unstable and stable condition, respectively. In addition, the difference in the normalized spectra at high frequencies was negligible, regardless of the stability condition. The Welch and the FFT spectra matched in the higher frequency range of the spectra, from frequency  $f$  above  $10^{-2}$  Hz, but in the lower frequency range the Welch spectra exceeded the FFT spectra. There was negative co-coherence for all the vertical separations, for the separations where large decay of the co-coherence was observed. For the separation between 37 and 40 m a.m.s.l, the negative co-coherence was small.

## **Acknowledgement**

To everyone who has encouraged me and helped me along the way to complete this thesis, I am eternally grateful. This endeavour would not have been accomplished without their direction, support, and encouragement. I owe a great debt of gratitude to Dr Charlotte, my supervisor, for all the help, encouragement, and direction she has given me. Her insightful comments and helpful criticism really improved the course and quality of this study. I owe so much to her for all her time, effort, and guidance.

I am thankful to the faculty and staff at the University of Stavanger, and particularly to the offshore technology department, for providing me with a supportive and challenging learning environment. Their funding and resources have been crucial to the success of this study.

Thanks to everyone who has helped me along the way, from coworkers to relatives to friends. Their ongoing support, thought-provoking conversations, and helpfulness have been invaluable. I appreciate them being in my life. I owe everything I am to my loving and supportive family. Their unwavering support, confidence in my abilities, and selflessness have allowed me to pursue higher education. Their support and faith in me have been invaluable, and I will be forever indebted to them.

In closing, I want to express my deep gratitude to everyone who has helped in any manner with this thesis. Thank you for all your help, encouragement, and direction; they have been invaluable. I appreciate your support and faith in me as we embark on this amazing adventure.

With heartfelt gratitude,

Osasenaga Igbinomwanhia

# TABLE OF CONTENT

Abstract: .....	i
Acknowledgement .....	ii
LIST OF FIGURES .....	vi
LIST OF TABLES .....	vii
1 Introduction .....	1
1.1 OBJECTIVES of STUDY .....	5
1.2 STUDY HYPOTHESIS.....	6
1.3 RESEARCH SCOPE .....	6
1.4 PROJECT OUTLINE .....	6
2 LITERATURE REVIEW .....	7
2.1 Wind Turbines .....	7
2.1.1 How a Wind Turbine Works.....	7
2.1.2 The Dynamics of a Wind Plant.....	8
2.2 Non-Neutral Conditions.....	12
2.3 Impact of atmospheric stability on turbine wake evolution.....	14
2.4 Deficit module’s turbulence intensity.....	15
2.4.1 Previous research works discussions on turbulent atmospheric boundary layer (ABL) 16	
2.4.1.1 Impact of ABL on wind turbine modelling, design, and output.....	18
2.4.1.2 Turbulence models and the modelling turbulence spectra .....	20
2.5 Theoretical Background.....	22
2.5.1 Monin–Obukhov Similarity Theory (MOST).....	22
2.5.1.1 Thermal Stratification of the Atmosphere using MOST .....	23
2.5.1.2 Assessing the credibility of MOST .....	24

2.5.1.3	One point turbulence spectrum.....	24
2.5.1.4	The Root- Coherence and Co-coherence of turbulence.....	25
3	METHODOLOGY .....	27
3.1	Site Description.....	27
3.2	Bockstigen observation data information .....	29
3.3	Data Processing.....	30
3.3.1	Categorization of the time series.....	30
3.3.2	Mean .....	30
3.3.3	Variance and Standard Deviation: .....	31
3.3.4	Max and Min Wind Speed .....	31
3.3.5	Stationarity test: .....	31
3.4	Power Spectra Density Using Welch vs FFT Method.....	34
3.4.1.1	Welch Method .....	34
3.4.1.2	Fast Fourier Transform (FFT) .....	35
4	RESULTS and DISCUSSION.....	36
4.1	Data description, Quality Assessment, and Numerical Simulations.....	36
4.1.1	Turbulence spectra .....	36
4.1.2	Coherence of turbulence .....	50
5	CONCLUSIONS and RECOMMENDATIONS.....	52
6	References .....	54
	Appendix A.....	61
	Appendix B.....	69

## LIST OF FIGURES

Figure 1-1: The normalized spectra of the Kaimal, ESDU, and API turbulence models were compared at wind speeds of 10 m/s and 50 m/s.....	2
Figure 2-1: Global wind installations in GW (source: Elgendi, 2023).....	7
Figure 2-2: Wind speed variation for surface roughness and turbulence in urban areas (Source: Tasneem et al., 2020).....	8
Figure 2-3: Wind turbine installations and capacity in Sweden compared to the world.....	8
Figure 2-4: Description of a Wind Farm and its components (Source: North Falls Offshore Wind Farm).....	9
Figure 3-1: The Bockstigen wind farm situated in Sweden (Source: Hansen, 2005).....	27
Figure 3-2: Orientation of meteorological mast and wind turbines.....	28
Figure 3-3: Position of Sensor on Wind Turbine 4 (Source: Goran Ronsten).....	29
Figure 3-4: Nominal Turbulence Distribution (Source: Goran Ronsten).....	30
Figure 3-5: (a: wind speed at 8m elevation;(b) wind direction at 8m elevation;(c) wind speed at 22m elevation; (d) wind direction at 22m elevation.....	33
Figure 3-6 (e: wind speed at 37m elevation; (f) wind direction at 37m elevation; (g) wind speed at 40m elevation; (h) wind direction at 40m elevation.....	34
Figure 4-1: Windrose: distribution of stability of wind speed.....	37
Figure 4-2: Frequency distribution of wind speed.....	38
Figure 4-3: Mean Wind speed distribution as a function of the Richardson number.....	38
Figure 4-4: Average PSD for wind speed 5-6 m/s.....	40
Figure 4-5: Average PSD for wind speed 6-7 m/s.....	40
Figure 4-6: Average PSD for wind speed 7-8 m/s.....	41
Figure 4-7: Average PSD for wind speed 8-9 m/s.....	41
Figure 4-8: Average PSD for wind speed 9-10 m/s.....	42
Figure 4-9: Average PSD for wind speed 10-11 m/s.....	42
Figure 4-10: Average PSD for wind speed 11-12 m/s.....	43
Figure 4-11: Average PSD for wind speed 12-13 m/s.....	43
Figure 4-12: Average PSD for wind speed 13-14 m/s.....	44
Figure 4-13: Average PSD for wind speed 14-15 m/s.....	44
Figure.4-14: Average spectra at 9m @ 3 conditions.....	45

Figure 4-15: Average spectra at 22.5m @ 3 conditions .....	46
Figure 4-16: Average spectra at 37 m @ 3 conditions .....	46
Figure 4-17: Average spectra at 40 m @ 3 conditions .....	47
Figure 4-18: Average spectra 1 conditions @ 4 heights .....	48
Figure 4-19: Average spectra unstable condition @ 4 heights .....	49
Figure 4-20: Average spectra Neutral condition @ 4 heights .....	49
Figure 4-21: Co-coherences of the along-wind velocity components at four different vertical separation distances. ....	50

## LIST OF TABLES

Table 1: Offshore wind turbine and its components .....	10
Table 2: Summary of wind speed measurements .....	29



# CHAPTER 1

## 1 INTRODUCTION

An exhaustive study of FOWTs' dynamic behaviour in reaction to aerodynamic and hydrodynamic loads under severe operating conditions across their design lifetime, as defined by the ULS, is necessary for their development. Dynamic reactions in FOWTs can be quite large in stormy sea conditions due to the presence of turbulent wind fields. Different turbulence models based on empirical data are recommended by different guidelines to deal with this issue.

According to IEC 61400-3:2009, extreme sea and wind conditions are those with a 50-year return period. A constant overall wind flow and the random fluctuations in wind speed due to turbulence describe these conditions. IEC 61400-3 (2019) states that a stationary random vector field is used to calculate offshore wind turbine load spectra for fatigue design, with each component assumed to follow a Gaussian distribution with zero-mean statistics. *Mechanical Fatigue of Metals: Experimental and Computational Perspectives*, pp. 383–390. The publishing house Springer has a global reach. Two turbulence models that can be used to calculate design loads are presented in the 2005 Geneva (Switzerland) International Electrotechnical Commission (IEC) 61400-1 standard. The spectrum and exponential coherence model, proposed by Kaimal (Kaimal et al., 1972), is the first. The second is Mann's (1994) uniform shear turbulence model. The Mann model is based on von Kármán's (1948) energy spectrum. Until a uniform velocity shear rapidly deforms this function, it is isotropic. While there is some overlap in terms of spatial coherence between the two theories, the energy frequencies at which they operate are distinct. Both turbulence models were developed with substantial help from data collected on the ground. Few turbulence models have been developed specifically for use with oceanic wind data (Cheynet et al., 2017).

Offshore structures are designed based on the (ISO, 19901-1, 2015) standard all over the world. This international standard has been used as a foundation for the development of national standards in the petroleum industries of the United States (API RP 2SK, 2005) and Norway (NORSOK N-003, 2007). Standards for the energy, maritime, and oil and gas industries have been produced by DNV GL, a classification society (DNV, G. 2019; Veritas, N. 2000; Veritas, 2021). Position mooring design guidelines are presented for extreme met-ocean conditions, including hydrodynamic and aerodynamic loads. The API turbulence model is recommended for the MBL,

whereas a 50- or 100-year return time is recommended for wind and waves. The API turbulence model is based on observations taken in the Norwegian municipality of Frya (Andersen and Lvseth, 1992). This spectrum is a modification of the Harris and Kaimal spectra (Taylor et al., 1971) that puts more weight on the low-frequency region while maintaining the correct high-frequency asymptote, as described by Andersen and Lvseth (2006). The API spatial coherence is derived from an expansion of the original exponential formulation by (Cheng & Chiu, 1990) and is thus analogous to the Kaimal coherence.

Research by Ochi et al., (1988) establishes that the low-frequency range (0.01 Hz) of offshore wind spectra collected since the late 1970s varies significantly, demonstrating the importance of tailoring the model to the individual site in question. Wind spectra have been found to differ between onshore and offshore locations, with the latter showing larger low-frequency components (Ochi and Shin, 1988; Shiotani, 1975; J.A.B. Wills et al., 1986). Thus, it may be necessary to choose an averaging time longer than the 10 minutes suggested by (IEC 61400-1, 2005). Normalized spectra comparisons at varying wind speeds for the Kaimal, ESDU (also known as the "improved von Kármán"), and API turbulence models are shown in Figure 1 of (RP-0286 2019).

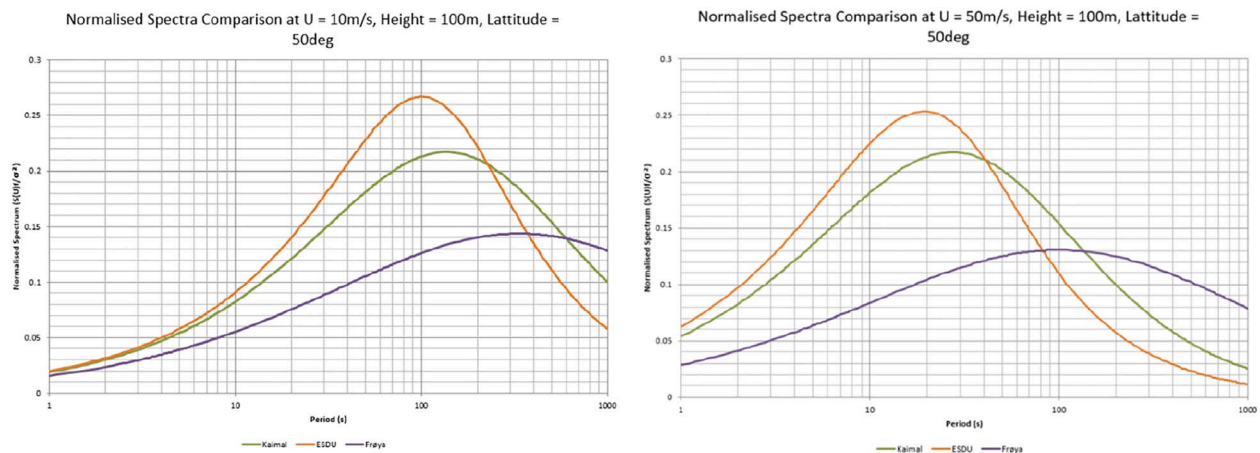


*Figure 1-1: The normalized spectra of the Kaimal, ESDU, and API turbulence models were compared at wind speeds of 10 m/s and 50 m/s.*

Results for the slower speed (10 m/s) are presented on the left, and results for the faster speed (50 m/s) are given on the right. The accuracy of the Frandsen model for estimating TI in wind farms is investigated here. Particularly for vast offshore wind farms, assessing the accuracy of such models is essential in light of the exponential increase in turbine size and the number of turbines in wind farms. In this study, the Frandsen model and a simplified version of the model are

compared to measured data from the Greater Gabbard offshore wind farm. The models that depended on individual turbine wake turbulence did better at predicting TI values than the Frandsen model, which relied on a model of ambient wind farms. That the model relied on variance in the turbulence of the freestream flow rather than predicting the variance in the turbulence generated by individual turbines explains why the observed mean and the 90th percentile values were different. This result needs to be backed up by more studies. For this reason, the authors conclude that accurate turbulence modelling in wind farms is essential for ensuring the health of turbines under conditions of stress and fatigue (Argyle et al., 2018).

While much effort has been put into building wake models to assess turbulence severity in offshore wind farms and anticipate wind speed reduction and power generation in wind farm arrays, very little work has been done to evaluate these models. The Frandsen model has not been extensively field-tested for its capacity to reliably estimate turbulence intensity, despite its initial development for calculating machine loads. Although calibrated using measurements from large eddy simulation models, the model has only been tested for estimating turbulence strength behind a single turbine. Semi-empirical models, such as the Frandsen model, are used to predict turbulence intensity in wind farm arrays, however this calls for more research (Calif & Emilion, 2012; Stevens & Meneveau, 2017).

Following in the footsteps of similar studies and delving deeper into the model, Frandsen and Madsen proposed the idea of Wake-Added Turbulence (WFT) in their investigation of the Nrrekaer Enge II wind farm, which proved a fair correlation between measurements above the rotor height and the WFT model. However, it was stressed that due to the location of the meteorological mast, the data should be evaluated with caution. The "Windfarm Assessment Tool" was created by applying Frandsen's WFT equation from the IEC 61400 standard to data from the Middelgrunden offshore wind farm to predict the severity of turbulence. The model did a good job of predicting the trend in the data, but it drastically under-estimated the values because it didn't take into consideration the effects of stability and proximity to land.

$$\sigma_{total}^2 = \sigma_0^2 + \sigma_{rotor}^2 \quad \text{Eq 1.1}$$

The standard deviation of wind speed and the velocity deficit were compared between models and measurements at the Wieringermeer test site in the Netherlands (Brand & Wagenaar, 2012). The study suggests that to get the entire variance of wind speed observed downstream of a turbine, one

needs to add the variance of the freestream wind speed (represented by a rough nodal square) to the variance of the wind speed generated by the turbine (represented by a rough rotor square). This was assumed to calculate the standard deviation of the wind speed.

The study found that the standard deviation of the induced wind speed was best estimated using a model that incorporated a power law function that dropped downstream of the rotor and two Gaussian peaks that emanated from the edges of the rotor in the span-wise direction. Eight rotor diameters downwind, these crests converged into a single peak. The early increase in standard deviation is suppressed by the rotor's thrust (Larsen, 2009). The results, however, demonstrated that the standard deviation was significantly underestimated due to several reasons. These included the omission of nacelle-generated turbulence, inaccurate model parameters for the decay of wake-generated turbulence, and the influence of freestream ambient turbulence intensity on the decay of additional turbulence.

In a wind tunnel, scale models of both straight and staggered turbines were put through their paces. Studies demonstrated that the turbulence strength plateaued after the sixth row of turbines in an aligned array, providing support for the use of a turbulence model that includes ambient wake. Maximum turbulence intensity was shown to not significantly increase beyond the first row in the staggered array (Chamorro et al., 2011), in part because of the prolonged recovery period of the wake from an upstream turbine. When comparing the two systems, it was found that the experimental values for turbulence intensity at hub height behind the eleventh row of turbines, representing wind farm-added turbulence intensity, agreed well with calculations using Equation below, after accounting for uncertainties in determining the experimental thrust coefficients.

$$\sigma_{add,wf} = \frac{0.36U_0}{1+0.2\sqrt{s_f s_r / C_T}} \quad Eq 1.2$$

The first two rows of turbines at the Lillgrund offshore windfarm were found to have significantly higher turbulence intensity levels when analysing wind directions with a 3.3D effective spacing, according to a study that used rotor effective wind speed (Göçmen & Giebel, 2016). However, this was the only noticeable rise. This lends credence to the recommendations made by the Frandsen model, which state that one must reach a certain distance inside the wind farm before the wakes have diffused sufficiently to establish an overall wind farm background turbulence intensity level.

The accuracy of the Frandsen model in relation to CFD simulations of wind farms has been studied. Large eddy simulations of a wind farm with 16 turbines in the streamwise direction were studied

by a group of researchers (Andersen et al., 2016) who used boundary conditions to offer an unlimited width in the lateral direction. Rarely were comparisons made between the Frandsen model and varying degrees of turbulence and wind speeds. According to the findings, the Frandsen model has good general performance but should be used with caution. The model accurately predicted the turbulence intensity in the far wake, but due to the blocking effects of the rotors, the turbulence intensity in front of each rotor was overestimated.

Finally, results from previous studies have revealed that the wind fields generated by LES and TIMESR display distinct differences across various atmospheric stability conditions. In unstable conditions, the wind shear is lower, the turbulence intensity is higher, and the structures are larger compared to neutral and stable conditions. Moreover, the unstable conditions exhibit more prominent coherent structures, which is evident from the coherence distributions in space and time. The frequency-dependent co-coherence values are higher in unstable conditions, and the first POD modes are significantly dominant. The wind fields generated by TIMESR and LES models are not completely representative of actual offshore wind conditions. More accurate measurements are required to better understand coherence in both vertical and horizontal directions, over distances that are relevant to modern offshore turbines. This will allow for more effective comparisons between models and real-world measurements. As wind turbine components are more affected by fatigue loads (Chambel et al., 2022) and unlike other offshore structures that are mainly affected by ultimate limit states and stress, this has led us to carefully consider the different effects of turbulence and how it affects the offshore wind turbine in a non-neutral condition.

## **1.1 OBJECTIVES of STUDY**

The aim of this study is to investigate and compare various non-dimensionalised spectrum models through the analysis of the Bockstigen wind data.

The specific objectives are:

- (1) To study the characteristics of the Bockstigen wind data;
- (2) To investigate the features of offshore turbulence in the frequency domain using the Bockstigen wind speed data.
- (3) To quantify and compare the observations and similarities between the co-coherence characteristics of offshore turbulence obtained from Bockstigen wind data at various heights.

## 1.2 STUDY HYPOTHESIS

It is possible to determine a turbulence model that would be suitable for use in an offshore environment under non-neutral conditions.

## 1.3 RESEARCH SCOPE

This study was carried out by analysing datasets from the Bockstigen wind farm. It entails the analysis of atmospheric stability and various turbulence spectral models for determining the most suitable model for the offshore environment under non-neutral conditions. To better design future offshore wind turbines in terms of fatigue reactions, we can compare our data (from Bockstigen) and build new offshore wind turbulence models.

## 1.4 PROJECT OUTLINE

This study is divided into 5 chapters:

- **Chapter 1:** Introduction- presents an introduction of the study. It highlights the motivation and problem statement of the study.
- **Chapter 2:** Literature review- reviews relevant literature on the turbulence models and their applications in offshore environment modelling. It presents background knowledge, basic theories, atmospheric stability, turbulence models of wind profiles, and discussions on past research works and relevant findings.
- **Chapter 3:** Methodology—describes the procedures that will be used to conduct the research. Methods for evaluating measurement data quality and selecting stationary velocity data are discussed.
- **Chapter 4:** Results and Discussion- presents and discusses the simulation results.
- **Chapter 5:** Conclusion- summarizes the findings and key observations.

# CHAPTER 2

## 2 LITERATURE REVIEW

### 2.1 Wind Turbines

In recent times, wind energy has become a crucial renewable energy resource to increase electrical power capacity; this is one reason for the surge in the global expenditures on renewable energy (Elgendi et., al, 2023). Renewable energy systems, such as solar, wind, hydro, and biomass, support the supply of energy demand while also boosting community development and environmental protection on a global scale. As wind energy has ranked amongst the most promising sustainable renewable energy sources, the amount of electricity available varies depending on wind conditions (speed, direction, etc.): this is the reason for the rise in studies to improve the effectiveness of harnessing wind energy more effectively (Elgendi et., al, 2023).

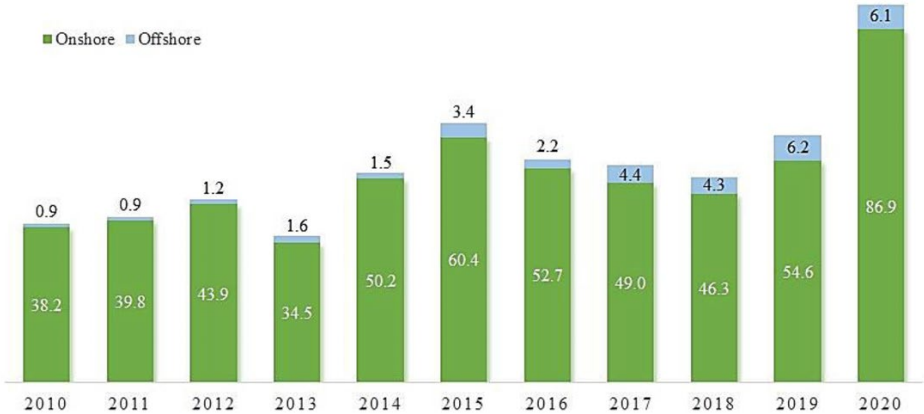


Figure 2-1: Global wind installations in GW (source: Elgendi, 2023)

#### 2.1.1 How a Wind Turbine Works

Wind turbines are devices that convert wind energy into electricity. They consist of a rotor, a nacelle, a tower, and other components such as a generator. There are several parameters that affect the technical performance of wind turbines which can include but not limited to wind speed, blade design, generator efficiency, tower height, air density, maintenance and repair, environmental conditions, etc. As proposed by Tasneem et al., (2020), to install a wind turbine, especially in urban areas, a careful environmental assessment is required to identify the best and most effective locations to install the turbines as depicted in Fig. 2 below.

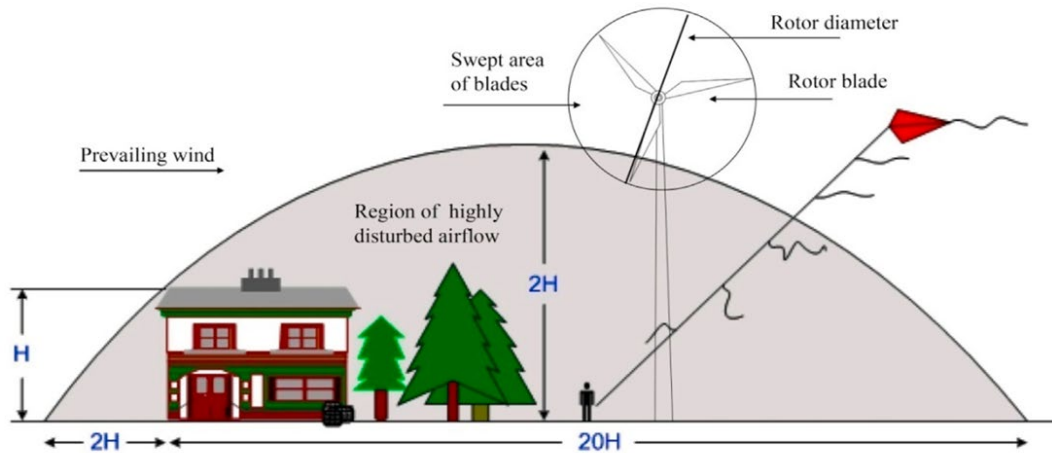


Figure 2-2: Wind speed variation for surface roughness and turbulence in urban areas (Source: Tasneem et al., 2020)

In Sweden, the growth of wind energy and the consequential wind farm development has been exponential. It was recorded by Enevoldsen and Permien (2018) that the yearly annual percentage increase was explosive than the 2006-2017 global development as shown in the figure below.

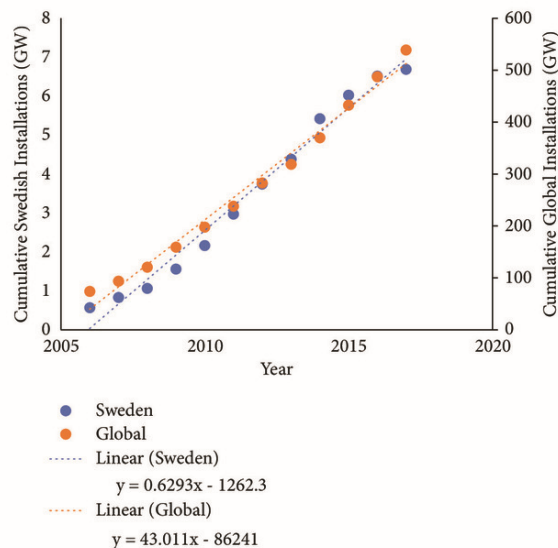


Figure 2-3: Wind turbine installations and capacity in Sweden compared to the world

### 2.1.2 The Dynamics of a Wind Plant

The wind plant combines an array of wind turbines in the same location to produce electricity. Factors that affect the location and placement of a wind farm includes, wind conditions, the surrounding terrain, access to the transmission of electricity, and other site related factors.



Normally each turbine generates electricity that is transmitted to a substation which in turn transfers it to the grid that powers the connected communities.

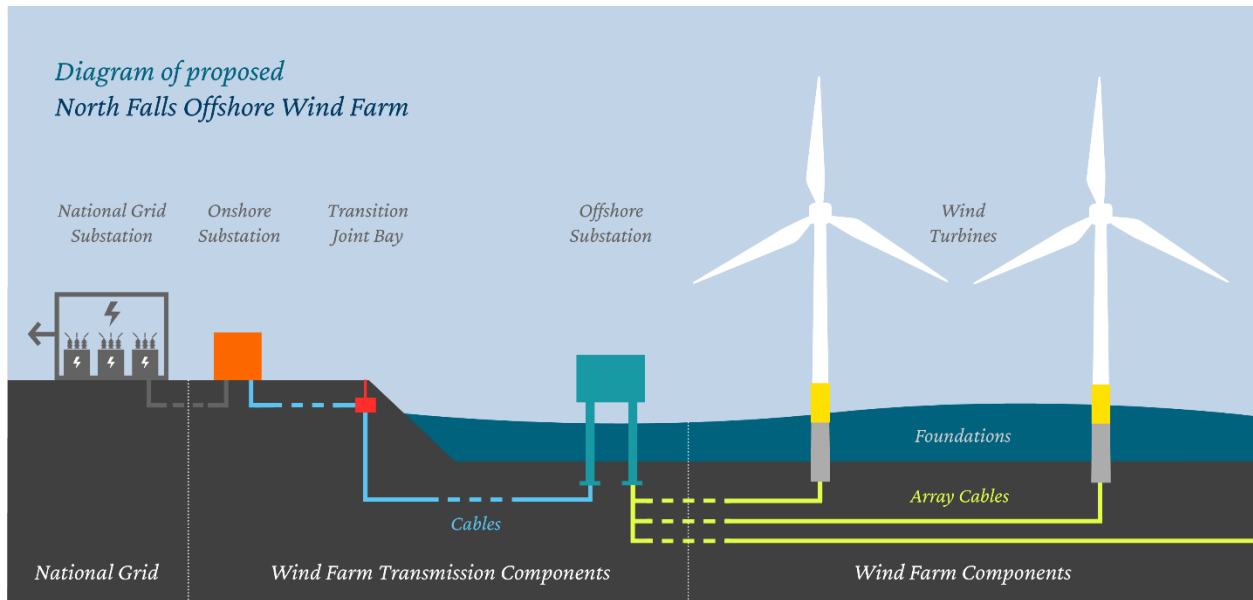
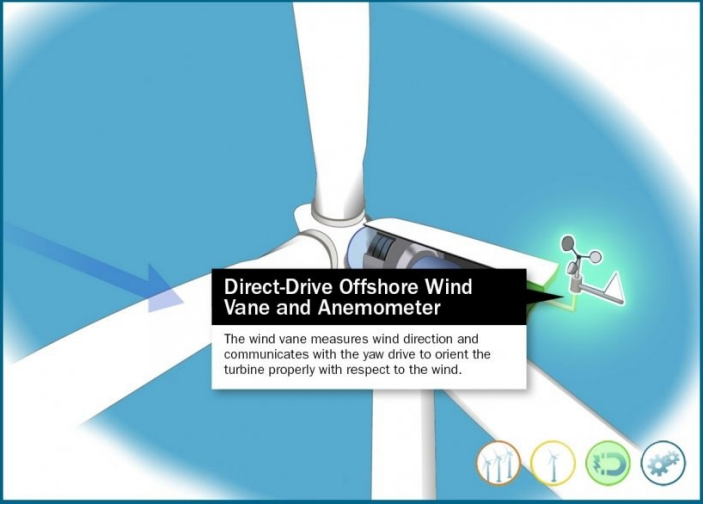
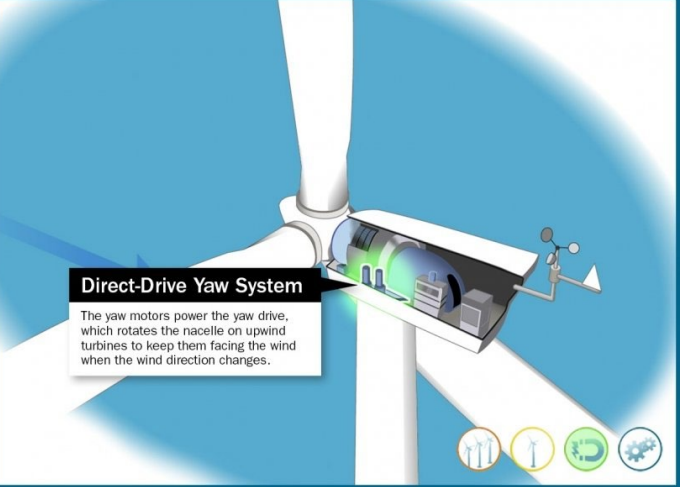
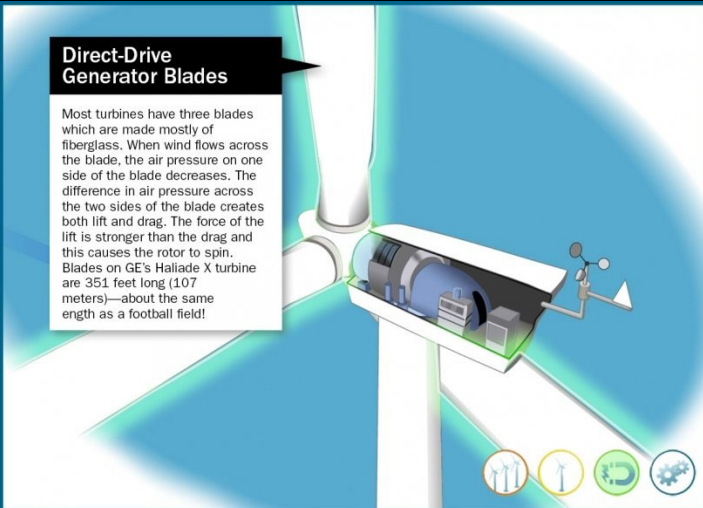


Figure 2-4: Description of a Wind Farm and its components (Source: North Falls Offshore Wind Farm)

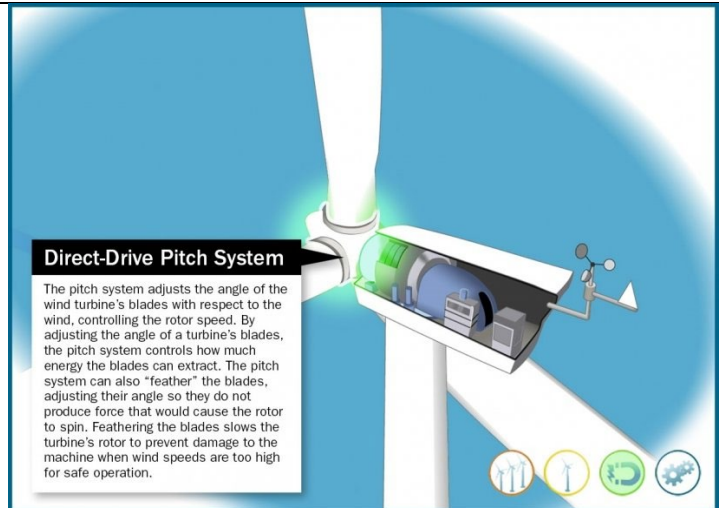
The modus operandi incorporates the transmission line, which transmits electricity at high voltages over long distances from the wind turbine to areas where such energies are dissipated or needed, the transformers receive steps up or steps down the alternating current received from the turbines to give out safe voltage for our buildings and homes. A substation is needed to function in the capacity of a link between the transmission system and the distribution system. The transformers mentioned earlier are placed within the substations.

Table 1: Offshore wind turbine and its components

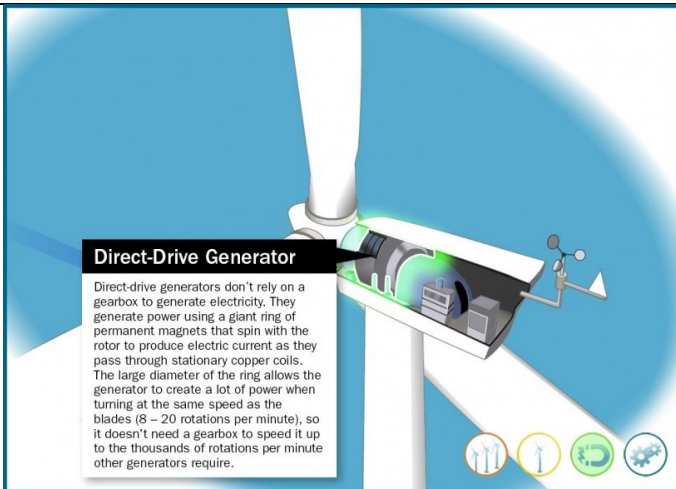
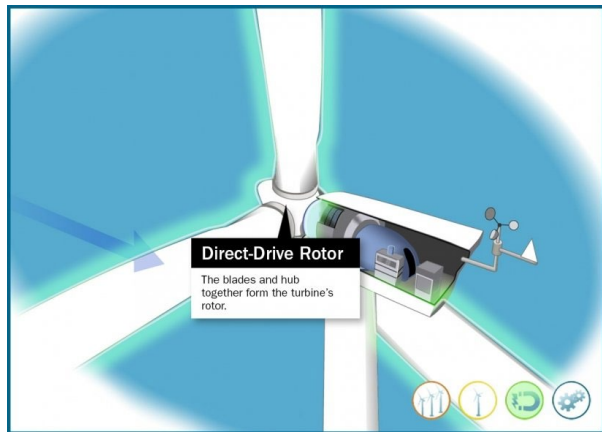
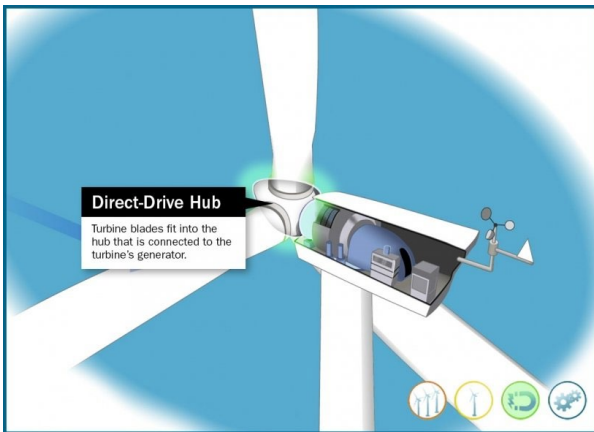
Direct Drive Offshore Wind Turbine and its Components (Source: US Department of Energy)	
 <p><b>Direct-Drive Offshore Wind Vane and Anemometer</b></p> <p>The wind vane measures wind direction and communicates with the yaw drive to orient the turbine properly with respect to the wind.</p>	<p><b>Wind vane and anemometer</b></p> <p>The wind vane detects the direction of the wind and relays that information to the yaw drive so that the turbine may be positioned to maximize energy production.</p> <p>The anemometer is responsible for tracking wind speed and relaying that information to the controller.</p>
<p><b>Yaw System</b></p> <p>This system orients the wind turbine rotor towards the wind direction</p>	 <p><b>Direct-Drive Yaw System</b></p> <p>The yaw motors power the yaw drive, which rotates the nacelle on upwind turbines to keep them facing the wind when the wind direction changes.</p>
 <p><b>Direct-Drive Generator Blades</b></p> <p>Most turbines have three blades which are made mostly of fiberglass. When wind flows across the blade, the air pressure on one side of the blade decreases. The difference in air pressure across the two sides of the blade creates both lift and drag. The force of the lift is stronger than the drag and this causes the rotor to spin. Blades on GE's Haliade X turbine are 351 feet long (107 meters)—about the same length as a football field!</p>	<p><b>Generator blades</b></p> <p>The blades of wind turbines typically consist of three fiberglass blades. One side of the blade experiences lower air pressure as the wind blows over it. Lift and drag are generated by the differential in air pressure between the blade's leading and trailing edges. The rotor spins because the lift force is more than the drag force. GE's Haliade X turbine has blades that are 107 meters (351 feet) in length, which is roughly the length of a football field.</p>

## The Pitch System

The pitch system controls rotor speed by changing the wind turbine's blade angle. The pitch system controls energy extraction by altering turbine blade angles. The pitch system can "feather" the blades to avoid spinning the rotor. Feathering the blades slows the turbine rotor to prevent damage at high wind speeds.



## Hub and Rotor

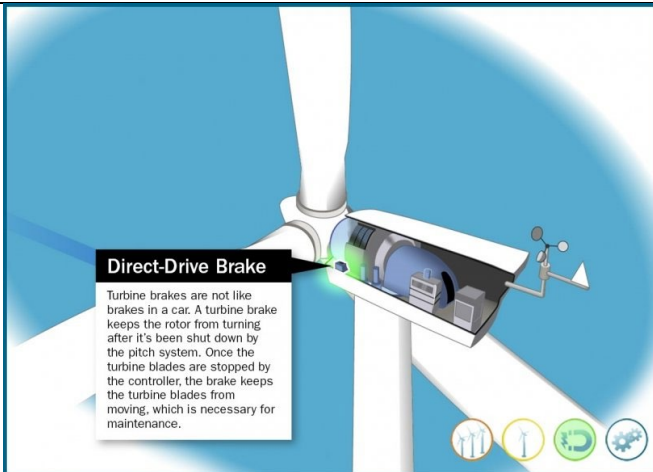
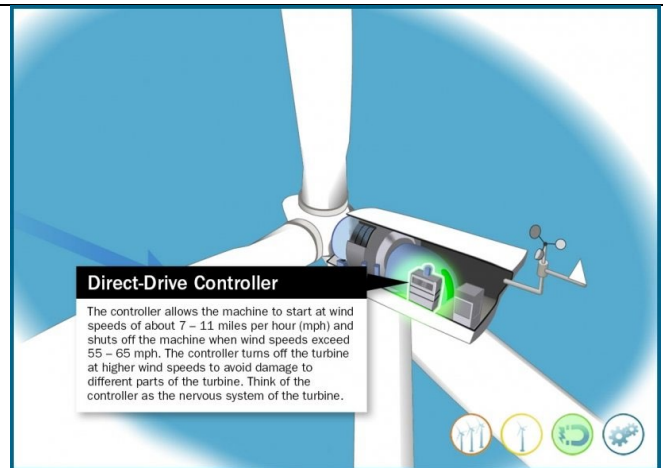


## The Generator

Direct-drive generators don't use gearboxes. A large ring of permanent magnets spins with the rotor to create electric current in stationary copper coils. The generator doesn't need a gearbox to speed up to thousands of rotations per minute since the ring's wide diameter allows it to generate a lot of power at the same speed as the blades (8-20 rpm).

## ***The Controller***

The sensor lets the machine start when the wind is blowing between 7 and 11 miles per hour (mph) and turns it off when the wind is blowing between 55 and 65 mph. At higher wind speeds, the controller turns off the turbine so that different parts of the turbine don't get damaged. The driver is like the turbine's nervous system.

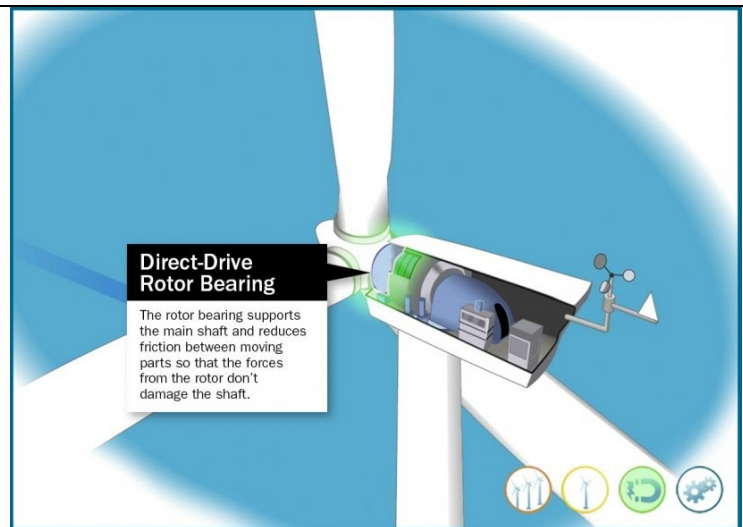


## ***Brake System***

The brakes on a turbine are not like the brakes on a car. The pitch system stops the rotor from turning, and a turbine brake keeps it from spinning. Once the controller stops the turbine blades, the brake keeps them from moving. This is needed for repair.

## ***Rotor Bearing***

The rotor bearing holds up the main shaft and lowers friction between moving parts so that the forces from the rotor don't damage the shaft.



## **2.2 Non-Neutral Conditions**

The DWM model is a wake model for wind turbines that was created initially in 2003 at the Ris Technical University of Denmark (Madsen et al., 2003, 2010; Larsen et al., 2008). When

simulating the wake deficit downstream from a wind turbine, the DWM model can be used as an efficient and computationally cheaper alternative to computational fluid dynamics. The purpose of this research is to improve our ability to predict wind turbine loads and power output by accounting for the large-scale wake meandering motion, a key driver of wind turbine fatigue stresses. Because large-scale movements of the wake deficit affect wind turbine loads differently than small-scale turbulence, it is not possible to accurately describe wake turbulence and its impact on wind turbines using a single turbulence intensity parameter, such as that used in the Frandsen model (Frandsen ST, 2007).

The DWM model is able to describe the impact of large-scale wake deficiency movements on wind turbine loads because it decomposes turbulence scales into two components. The model assumes that the meandering of the wake, caused by large turbulent scales, may be examined independently from the growth of the wake deficit. Using the wake deficit model proposed by (Ainslie, 1986, 1988), the dynamic wake meandering (DWM) model estimates the typical wake flow trailing a wind turbine. The Navier-Stokes equations are approximated using a thin shear layer with a straightforward eddy viscosity formulation as the basis for this model. However, (Keck et al., 2011) presented an enhanced eddy viscosity model that combines a two-dimensional eddy viscosity model into the DWM, which more accurately depicts the radial distribution of the turbulent energy. By properly characterizing the turbulence scales, this change allows for more precise projections of the loads on and output from wind turbines.

The DWM model incorporates a wake-added turbulence expression to account for the extra turbulence generated in the wake shear layer. Although Madsen et al.'s (2005) implementation of a wake-added turbulence formulation based on the local depth and the radial gradient of the wake deficit accurately accounts for additional mechanical loads caused by small-scale turbulence, this correction is not coupled to the wake deficit evolution and has no effect on the development of downstream rotor wakes. Keck et al. (2012) proposed a different method for detecting wake-added turbulence, in which turbulent stresses in the preceding wake are used to determine the wake turbulence intensity level at the subsequent downstream turbine. A bigger amount of turbulence is built up over a wind farm because this formulation connects the wake-added turbulence to the wake deficit evolution at the downstream rotor.

### **2.3 Impact of atmospheric stability on turbine wake evolution**

Considering this, the developers of the DWM model set out to develop a model that accounts for the influence of air stability on the evolution of the turbine wake. Previous research has proven that air stability influences wake evolution. In the 1980s, air stability was investigated as a potential cause of wandering wakes (Ainslie, 1986). However, as stated by (Barthelmie et al, 2009), few existing engineering wake models consider the impacts of air stability.

A wind farm's wake effects were found to be considerably influenced by atmospheric stability, even when the intensity of the ambient turbulence was held constant. The primary goal of this research was to determine if, after including the recommended changes, the DWM model can effectively account for the impact of non-neutral atmospheric stability on power generation. These results suggest that it is misleading to describe wake dynamics in the ABL just in terms of turbulence strength, and that the effect of air stability on the turbulent length scale is essential to comprehending the behavior of wind farms. It also means that the flow component in the mean wind direction is not sufficient for determining turbulence intensity, and that all three components must be taken into account. In particular, the published data reveal that atmospheric stability influences the meandering of the wake and the evolution of the wake deficit via influencing the length scale of air turbulence. In addition, the study discovered that air stability has a substantial effect on the Annual Energy Production (AEP) of a wind turbine affected by a single wake. Even if the strength of the surrounding turbulence is held constant, the wake effects in a wind farm will still be affected by stability. This shows that the turbulent length scale, which is controlled by air stability, plays an important role in the dynamics of wind farms, and that turbulence intensity alone is not adequate to reflect wake dynamics in the ABL. For highly unstable to very stable conditions, the air stability can affect the AEP of a wind turbine by as much as 0.50%, which is about equivalent to 25% of the AEP loss due to the wake. This seemingly small percentage could end up saving a large wind farm millions of dollars. Therefore, it is crucial to incorporate stability effects into the DWM model in order to get accurate estimations of AEP. Field measurements and simulations of the North Hoyle and OWEZ wind farms show that the power output of a row of wind turbines facing the same direction as the wind is reduced by about 10% in highly steady conditions compared to very unstable ones (Keck et al., 2013).

## 2.4 Deficit module's turbulence intensity

The DWM model incorporates wake-added turbulence to account for the impact of the small-scale turbulence created by the shear layer in the wake of the downstream turbine. The downstream turbine's wake evolution, loads, and induction are all influenced by the turbulence. To quantify the turbulence contribution of the wake, turbulent stresses are explicitly estimated as part of the wake deficit calculation as proposed by Larsen (2009).

$$TI_{DWM\ MFOR} = \max\left(\sqrt{\frac{1}{C_{u'w'} \left(\frac{w'_{rms}}{u'_{rms}}\right)}} \times \tau_{stress\ DWM}, TI_{amb}\right) \quad \text{Eq. (2.1)}$$

The coefficient  $C_{u'w'}$  and the ratio  $w'_{rms}/u'_{rms}$  are utilized to characterize the relationship between the axial and radial turbulent fluctuations in the wake because of the shorter length scale and increased anisotropy of wake turbulence. We used a  $w'_{rms}/u'_{rms}$  ratio of 1, based on prior work by Larsen, and a correlation coefficient of 0.3.

The wake deficit of a DWM may be computed using the momentum equation, which looks like this:

$$u \frac{\partial u}{\partial x} + v \frac{\partial u}{\partial r} = \frac{1}{r} \frac{\partial}{\partial r} (v_T r \frac{\partial u}{\partial r}) \quad \text{Eq. (2.2)}$$

Its stability is defined by the equations shown above, which involve the radial component ( $r$ ) of the velocity ( $u$ ) and the mean flow direction ( $x$ ) of the velocity ( $v$ ). To take turbulent diffusion into consideration, we employ the eddy viscosity ( $v_T$ ). This is accomplished by employing an equation describing a mixing length model in a dimensionless form.

$$r \frac{\partial}{\partial r} (rv) + \frac{\partial u}{\partial x} = 0 \quad \text{Eq. 2.3}$$

In the similar context of non-neutral conditions for offshore environment, despite the well-known fact that unstable atmospheric stability conditions can cause higher turbulence, proper turbulent wind models for unstable conditions are not commonly used in simulating the loads and motions of offshore wind turbines. The authors simulated a spar-buoy offshore wind turbine (OWT) using their own Hjstrup model, which was developed specifically for unstable conditions. This allowed them to examine the importance of unstable conditions in the design of floating offshore wind turbines. The results show that unstable conditions have a major impact on the fatigue damage of a spar-buoy OWT, with very unstable conditions leading to 65% higher fatigue damage than

neutral conditions when discussing top tower torsion, followed by 37% greater fatigue damage when discussing base tower side-side bending, and finally 24 percent greater fatigue damage relevant to blade root flap-wise configuration. According to the findings, the turbulence intensity can increase by as much as 40 percent when a proper wind model is used for unstable atmospheric circumstances. Floating offshore wind turbines (FOWTs) must account for such situations in their design because they are so widespread in the ocean. The development and validation of a turbulent wind model that can account for unstable conditions in the offshore marine boundary layer is crucial for reducing the inherent risk in the design of large FOWTs. Therefore, the study emphasizes the need to account for variable weather conditions in FOWT designs and the creation of suitable wind models (Putri et al., 2019).

#### **2.4.1 Previous research works discussions on turbulent atmospheric boundary layer (ABL)**

The typical offshore environment is characterized by stable wind conditions and low turbulence levels. However, things change drastically once you enter a wind farm, as the flow becomes quite turbulent. As the number of offshore wind farms increases, it is essential that their internal flow characteristics be well understood. This knowledge is essential not only for optimizing the farm's performance but also for increasing the lifespan of individual turbines. Improved understanding of the flow characteristics inside offshore wind farms can aid in the development of effective models to represent the flow in the downstream region. Studying the flow characteristics in a wind farm can be facilitated by such models in a timely and productive manner. Considering this, researchers at Bockstigen investigated the role that generated turbulence plays in the evolution of flow along a long line of wind turbines in pursuit of a wake deficit asymptote. The study makes use of EllipSys3D, a computational fluid dynamics tool that employs a finite volume technique to solving the incompressible form of the Navier-Stokes equations. Turbulence is modelled using the Large-Eddy Simulation technique, and wind turbine rotors are modelled as actuator discs whose loading is determined by applying the blade-element method to tabulated air foil data.

This study reports that imposed turbulence and wind turbine rotors influence the flow characteristics along a row of ten turbines spaced by seven rotor diameters, as is customary in offshore wind farms. The Mann model generates two predetermined turbulence intensities, at 4.5 and 8.9 percent. The turbines are protected from the environment, and a non-sheared intake is utilized, to prevent interference from the air boundary layer. The forced turbulence and the rotors' presence will be considered, but the focus will be on the flow's inherent features. The flow



characteristics are studied by taking readings of several statistical measures, such as the standard deviation, the kinetic energy of turbulence, the mean velocity, the power spectrum of axial velocity fluctuations, and the mean power generation along the turbine row. This research provides important information that can be used to improve the efficiency and effectiveness of wind farm design by shedding light on flow behaviour and turbine performance in the presence of generated turbulence.

The models now include a generator torque controller for low-flow circumstances and rated-power operation. The study plotted the standard deviation of velocity components, kinetic energy of turbulence, power, and mean velocity as a function of downstream distance to highlight the flow characteristics. Ten of the turbines in the row reached an asymptotic wake state under the experimental conditions. In addition, accelerating the transition in the domain by introducing disturbance. The power spectra of axial velocity fluctuations helped shed light on turbulence (Breton et al., 2014), but they were ineffectual when it came to identifying if an asymptotic wake state had been attained.

The surface fluxes between the land and the atmosphere are significantly influenced by the turbulent atmospheric boundary layer (ABL). Interactions between the ABL flow and individual turbine wakes are also complex in wind farms (Goit & Meyers, 2015). Large-eddy simulations (LES) have been utilized to explore land-ABL interactions and wind farm-ABL interactions to better understand the underlying flow mechanics (Anderson et al., 2012). These simulations have been crucial in helping scientists make sense of the myriad ways in which wind farms and the ABL flow interact.

The spatial and temporal resolution of significant turbulent-flow fluctuations in wind farm-atmospheric boundary layer (ABL) interactions can be accurately modelled using the large-eddy simulation (LES) method. These variations have a significant impact on design and operation considerations for wind farms, including fatigue loading of turbines and variations in power output. Wind energy research has made considerable use of LES for standard wind farm instances, including those with periodic boundary conditions, constant flow forcing, and a constant mean wind direction (Porté-Agel et al., 2011). The asymptotic limit of such systems can be better understood with the help of simulations of huge wind farms. However, the impacts of wind turbines on the incoming flow, as well as the spatial evolution of the flow in finite-length wind farms, must be considered. The existence of wind turbines does not negate the need for actual

inflow conditions to be included when modelling such systems. The significance of these stipulations has been previously established (Stevens et al., 2014).

#### **2.4.1.1 Impact of ABL on wind turbine modelling, design, and output**

While turbulence in the atmospheric boundary layer (ABL) can affect the power production of wind turbines, the effect is reduced when many turbines are distributed across a large region due to the limited spatial correlation and small length scales of the turbulence. Extreme power fluctuations occur throughout the entire wind farm due to variations in wind speed and direction caused by mesoscale meteorological processes such as cellular convection and weather fronts, which have length scales of 10 to hundreds of kilometres and associated timescales of tens of minutes to several hours (Ray PS, 1986). According to LES research on wind farms (Porté-Agel et al., 2013), even a small shift in mean wind direction can have a large impact on the wake conditions of downstream turbines, leading to a noticeable shift in wind farms' aggregate power output. Therefore, it is vital to incorporate large-scale mean-flow transients in wind-farm LES to accurately anticipate power under actual meteorological conditions.

Considering these studies, authors performed a study where the concurrent precursor method is applied to a practical example that highlights the importance of inflow direction variability in wind farm modelling, especially for those situated in atmospheric boundary layers (ABLs) with possible mesoscale variations. However, application of precursor techniques is limited in scenarios where the mean inflow direction is variable. Researchers have designed and implemented a novel variable-direction precursor approach in the SP-Wind LES solver (Meyers & Meneveau, 2010) to address this limitation and improve the solver's capability to handle flow scenarios with varying inflow directions. In situations when the mean-flow direction varies, the newly developed variable-direction precursor method allows turbulence-resolving simulations to have fully formed turbulent inflow conditions. This can be accomplished without increasing the already low computing expenses of traditional precursor methods. If the rate of change in the flow direction is not excessively quick in comparison to the turbulence time scales in the major domain of interest, the method can be applied to both LES and DNS. Because of this, the method can be applied to a wide variety of scenarios involving varying inflow rates and directions.

The growth of wind energy in recent years has inspired hope that it may soon make a substantial contribution to satisfying the global need for electricity. Increasing wind power penetration and making the switch to a sustainable energy system, however, requires the construction of large-

scale onshore and offshore wind farms due to wind power's notoriously low power density. Recent study has focused on the interplay between wakes generated by huge wind turbines and highly variable air flow phenomena that occur on an even greater scale to better understand the flow and turbulence phenomena that occur in these extended wind farms.

Each component must be considered independently if the complex multiscale system of wind energy is to be comprehended. Individual wind turbine design and optimization are well-studied and developed fields (Snel, 1998; Burton et al., 2001; Herbert et al., 2007), especially for big horizontal-axis turbines. The aerodynamics of horizontal-axis wind turbines were reviewed in detail by Srensen in 2011, and the structure of wakes caused by individual turbines has been the subject of numerous studies. Models that characterize the wake structure of a single wind turbine are typically used in conjunction with methods that consider the interaction and superposition of numerous wakes in the design and optimization of wind farms. The use of Reynolds-averaged Navier-Stokes (RANS) flow models, which have been extensively studied for wind turbines and wind farms by (Vermeer et al., 2003; Sanderse et al., 2011), is also common.

Researchers have taken a broader view of the atmosphere to learn more about wind turbine arrays. By taking a roughness element model, like in Newman (1977) and Meneveau (2012), wind turbine arrays can be studied in a new light. These findings have been incorporated into models examining the regional and global impacts of massive wind farms on weather and climate (Zhou et al., 2012).

Considering the aforementioned, the wind turbine array boundary layer (WTABL) has developed as a distinct type of boundary layer flow in wind farms, and a thorough understanding of individual wind turbine wakes and the atmospheric boundary layer is required for optimal design and operation. To further understand the underlying flow dynamics, the literature on wind tunnel experiments, field observations, and computational and theoretical developments is required. Large Eddy Simulation (LES) and Reynolds-Averaged Navier-Stokes (RANS) models are used to compute the mean three-dimensional velocity distributions and temporal fluctuations, with the latter coming at a high computational cost due to the lack of a general theory of the superposition of canonical turbulent shear flows. By summarizing these results, we gain a deeper understanding of the interplay between WTABL's components and their implications for optimizing wind farms.

Quick prediction methods based on analytical or simplified numerical models are needed for effective wind farm design. Some such models are highlighted in the papers, and comparisons to

experimental and simulated data are made. Multiple wakes interacting with the atmospheric boundary layer (ABL) and a free wake in a turbulent environment are used in the analytical models. These models account for the separate flows' turbulent kinetic energy and modify flow parameters like the wake expansion coefficient to replicate the ABL's behaviour at a broader scale. Analytical models can be evaluated for use in real-world engineering design by comparing them to data from experiments and simulations (Stevens et al., 2017).

To describe the wind characteristics of an offshore wind turbine, the current standards suggest using a very simple turbulence model (IEC 61400-1, 2005). These simulations are grounded in data gathered from studies of wind over land, small turbines, and stationary bases. As the rotor size of offshore wind turbines continues to grow (Golston et al., 2019), the importance of the wind's temporal and spatial change over the rotor diameter rises. The nominal rotor frequency of roughly 10 revolutions per minute for big, bottom-fixed, offshore wind turbines is the lowest relevant frequency for load analysis. Taking into consideration natural modes associated to stiff body motions is essential while designing floating wind turbines. The six rigid body types of motion can have natural periods anywhere from a few seconds to more than a hundred seconds, depending on the design. The description of the wind field is complicated by these low-frequency natural periods. To obtain realistic loads, the turbulence's low-frequency turbulent energy and spatial organization must be accurate.

#### **2.4.1.2 Turbulence models and the modelling turbulence spectra**

The Kaimal spectral (Kaimal et al., 1972) and exponential coherence model (IEC 61400-1, 2005) or the Mann spectral tensor model (IEC 61400-1, 2005) are two turbulence models recommended by the International Electrotechnical Commission (IEC) wind turbine design standard. When it comes to low frequencies, however, which are crucial for floating wind turbines, studies have shown that the choice of turbulence model can have a considerable impact on the response of a wind turbine. Therefore, evaluating how well these two models depict offshore wind fields is crucial.

The reaction of a wind turbine is greatly affected by the wind characteristics measured at the hub height, such as wind speed and turbulence intensity (TI) (Robertson et al., 2018). However, as rotor diameters increase, knowledge of the wind field's spatial and temporal dispersion becomes more crucial. Both wind shear (the difference in average wind speed at different heights in a rotor) and coherent structures have significant roles. Analysing the correlation in frequency space, or

coherence, allows us to see coherent patterns at work throughout a range of separation distances. The rotor plane can be analysed with proper orthogonal decomposition (POD) to find coherent structures.

While all standardized turbulence models provide wind fields with the same point statistics and shear, the coherence and POD modes might vary from one model to the next (Bachynski & Eliassen, 2018; Doubrawa et al., 2019). Eliassen and Obhrai (2016) reviewed previous research that compared turbulence models to offshore data, with an emphasis on spectra and coherence. The North Sea offshore mast FINO1 (FuE-Zentrum FH Kiel GmbH) provided data for these analyses, which offers crucial insights into the offshore wind field. Measurements, however, should not be taken as the "truth" because they can only be taken at a small number of points in space and need to go through processing and quality assurance before being used. The TIMESR function in TurbSim (Kelley N. et al. 2023), for example, can be used to build wind field simulations from point observations, but doing so requires making a number of assumptions and simplifications.

Large-eddy simulations (LES) are a more sophisticated alternative to the simple turbulence models specified by the standard for generating wind fields. Solving the equations of momentum and pressure is a computationally intensive step in this method. Wind fields produced by LES have been compared to those produced by the Kaimal and/or Mann models in a number of studies (Doubrawa et al., 2019; Simley & Pao, 2015; Berg et al., 2016). Comparing these models with LES allows for the evaluation of lateral coherence and proper orthogonal decomposition (POD) modes, which cannot be measured through point measurements.

Although there is considerable leeway for changing turbulence strength to non-neutral circumstances, the turbulence models recommended by the IEC design standard are largely intended for neutral stratification. This, however, ignores the reality that other conventional parameters continue to be the same no matter the state of atmospheric stability. Several studies (Sathe et al., 2007; Holtslag et al., 2016) have shown that the wind profile and turbulent structure of the wind field are significantly affected by air stability, and hence the dynamic response of wind turbines. Therefore, it is essential to compare these reference models to observations or LES for different states of atmospheric stability. This is especially important for offshore wind turbines, as they operate in environments with less turbulence and wake recovery is very sensitive to stability.

As a result, research has been done to assess whether the Mann and Kaimal turbulence models, as suggested by the IEC design standard, are adequate for forecasting wind turbine response and weather conditions. The evaluation relies on a comparison of the reference wind fields to both offshore measurements and Large-Eddy Simulations (LES) run with the SOWFA simulation program (Churchfield et al.). Standard turbulence models and their industrial applications are thoroughly described and tested in this paper, with results broken down by atmospheric stability conditions and wind speed. The turbulence intensity and wind profile are modified to fit stable or unstable conditions, however the neutral flow assumed by the Kaimal and Mann spectral formulas is not considered in this investigation. Each technique is simulated nine times, once at each of three different wind speeds (below, at, and above the rated speed) and three different atmospheric circumstances (unstable, neutral, and stable). The study's objective was to examine the impact on the dynamic response of big offshore wind turbines of using different turbulence models to mimic wind fields under varying atmospheric stability conditions. Important for turbine response are spatial and temporal variations in coherence and POD modes, which are the focus of this analysis. It employs the generated wind fields for dynamic response analysis to better understand the capabilities of the baseline turbulence models. It took just over an hour of simulations to capture all the important frequencies produced by both land-based and offshore wind farms using massive turbines. For load balancing reasons, 200 extra seconds will be added. The DTU 10-MW reference turbine (Bak et al., 2013) was chosen to maintain uniformity; it has a diameter of 178.3 m, a hub height of 119 m, and a rated wind speed of 11.4 m/s.

## **2.5 Theoretical Background**

### **2.5.1 Monin–Obukhov Similarity Theory (MOST)**

The Monin-Obukhov similarity theory (MOST) provides expressions for estimating the vertical profiles of wind speed, temperature, and humidity in the atmospheric surface layer, which is the layer of the atmosphere that is directly influenced by the Earth's surface. It considers the effects of buoyancy, which arise from the heating or cooling of the surface, and shear, which arises from wind speed variations with height (Putri et al., 2022).

Monin-Obukhov theory has numerous applications in atmospheric science and meteorology, including weather prediction, climate modelling, air pollution studies, and agriculture. It is used to estimate fluxes of heat, moisture, and momentum at the Earth's surface, and to understand the dynamics of the atmospheric boundary layer, which is the lowest part of the atmosphere that

interacts directly with the surface. It is an important tool for understanding and predicting the behaviour of the atmospheric surface layer, which has significant impacts on weather, climate, and human activities.

The average ( $\bar{u}$ ,  $\bar{v}$ ,  $\bar{w}$ ) and the fluctuating ( $u'$ ,  $v'$ ,  $w'$ ) parts of the along-wind, crosswind, and vertical velocity components are denoted by  $u$ ,  $v$ , and  $w$ , respectively. The theory works on the assumption that  $\bar{v}$ , and  $\bar{w}$ , are close to zero on smooth, uniform surfaces. This model requires the random processes making up the fluctuations to be stationary, Gaussian, and ergodic (Monin, 1958).

Power spectral density (PSD) and root coherence modelling of the 'v' component may be required for asymmetrical flow situations even though the 'u' component is what drives the rotor fatigue stresses (Sanchez Gomez and Lundquist, 2020). When the wind is blowing from different directions, it can cause a skew in the flow. Mouzakis et al. (1999) argued, however, that the vertical velocity component is more important for fatigue load estimate in wind turbines.

### 2.5.1.1 Thermal Stratification of the Atmosphere using MOST

The thermal classification is stratified by

$$\xi = z/L \quad \text{Eq. (2.4)}$$

Where  $z$  = height above the surface

$$L = \frac{u_*^3 \bar{\theta}_v}{gk(\overline{w'\theta'_v})} = \text{Obukhov Length (Monin and Obukhov, 1954)} \quad \text{Eq. (2.5)}$$

$u_*$  = friction velocity (Scaling velocity)

$\bar{\theta}_v$  = mean virtual potential temperature

$G = 9.81\text{m/s}^2$

$k \approx 0.4$  = von Karman constant

$\overline{w'\theta'_v}$  = vertical flux of virtual potential temperature.

Putri et al., 2022, suggested a method for obtaining  $\overline{\theta'_v}$  which includes.

- (1) Approximating it by the fluctuating sonic temperature measurement
- (2) If it cannot be derived from sonic anemometers, then it could be obtained from the absolute temperature recordings. This temperature data was converted from pressure data.

The friction velocity above can be computed as follows. Eq. (2.5)

$$u_* = \sqrt[4]{u'w'^2 + v'w'^2}$$

### 2.5.1.2 Assessing the credibility of MOST

- (1) By studying the non-dimensional mean wind speed profile
- (2) The validity of MOST is affected by the presence of waves.
- (3) If there are internal boundary layers, and the fetch is several kilometres in length.

$$u_* = u^0 W^0 + v W^0 \quad \text{Eq. (2.6)}$$

$$\phi_m \left( \frac{z}{L} \right) = \frac{kz}{u_*} \frac{\partial \bar{u}}{\partial z} \quad \text{Eq. (2.7)}$$

Where

$$\phi_m \approx \begin{cases} 1+15.2|\zeta|^{-1/4}, & -2 \leq \zeta < 0 \\ 1+4.8(\zeta), & 0 \leq \zeta < 1 \end{cases}$$

[As empirically presented by Hogstrom (1988)]

### 2.5.1.3 One point turbulence spectrum

Below is presented the normalised surface layer one-point velocity spectra and how it expresses a universal behaviour in the inertial subrange.

$$\frac{f S_u(f)}{u_*^2 \phi_\epsilon^{2/3}} \approx 0.3 f_r^{-2/3} \text{ at } f_r \gg 1 \quad \text{Eq. (2.8)}$$

$$\frac{f S_v(f)}{u_*^2 \phi_\epsilon^{2/3}} \approx \frac{f S_w(f)}{u_*^2 \phi_\epsilon^{2/3}} \approx 0.4 f_r^{-2/3} \text{ at } f_r \gg 1 \quad \text{Eq. (2.9)}$$

$S_u$ ,  $S_v$ , and  $S_w$  are the velocity spectra for the along-wind, crosswind, and vertical velocity components, where  $f$  is the frequency and  $S_u$ ,  $S_v$ , and  $S_w$  are the corresponding spectra.

Non-dimensional turbulent kinetic energy dissipation rate Eq. (2.10)

$$\phi_\epsilon = \frac{kz\epsilon}{u_*^3} \quad \text{by Wyngaard and Cote, 1971}$$



$\epsilon$  is the rate of dissipation of kinetic energy in turbulent flows.

$$\sigma_\epsilon^{2/3} = \begin{cases} 1 + 0.5|\zeta|^{2/3}, & \zeta \leq 0 \\ (1 + 5\zeta)^{2/3} & \zeta \geq 0 \end{cases} \text{ by Kaimal and Finnigan, 1994; Putri et al., 2022} \quad \text{Eq. (2.11)}$$

#### 2.5.1.4 The Root- Coherence and Co-coherence of turbulence

One of the primary characteristics for the structural design of wind turbines is the root coherence, which is defined as the normalized cross-spectral density of turbulence and has a complex valued entity; the real part is called the co-coherence.

The co-coherence at vertical separations  $\gamma_i$  where  $i = \{u, v, w\}$  is described thus Eq. (2.12)

$$\gamma_i(z_1, z_2, z_3, f) = \frac{\text{Re}[S_i(z_1, z_2, f)]}{\sqrt{S_i(z_1, f)S_i(z_2, f)}} \quad \text{by IEC 61400-1, 2005}$$

$S_i(z_1, z_2, f)$  = density of the cross-spectrum at two points,  $z_1$  and  $z_2$ , at elevations  $z_1$  and  $z_2$ .

$S_i(z_1, f)$  = one-point spectra estimated at  $z_1$

$S_i(z_2, f)$  = one-point spectra estimated at  $z_2$

The following presents an empirical model for characterizing the coherence for vertical separations:

This empirical model was proposed by Davenport (1961)

$$\gamma_i(n) \approx \exp(-c^i n) \quad \text{Eq. (2.13)}$$

Where  $n$  (reduced frequency) =  $\frac{2fd_z}{\bar{u}(z_1) + \bar{u}(z_2)}$

$d_z = |z_1 - z_2|$ . At three different heights  $z_1 > z_2 > z_3$ , such that  $z_1 - z_2 = z_2 - z_3$ .  $c^i$  was described as a decay parameter.

The Davenport's equation was later modified by Bowen et al. (1983) were he assumed a linear decay function.

$$c^i = c_1^i + \frac{2c_2^i d_z}{(z_1 + z_2)}, \quad \text{Eq. (2.14)}$$

As seen in the preceding equation 2.14, the coherence can grow with increasing height of measurement if the signal is blocked by the ground or a surface. Particularly when the data are coupled with huge separations, the co-coherence may diminish at a faster rate than predicted by Davenport's model. Equations 2.15–2.17 are the result of a later change to Equation 2.14 by Bowen et al. (1983), which introduced a third decay parameter.

$$\gamma_{ii}(z_1, z_2, f) = \exp(-f_a) \exp(-f_b) \quad \text{Eq. (2.15)}$$

$$f_a = \frac{|z_2 - z_1|}{\bar{u}(z_1, z_2)} \sqrt{(c_1^i f)^2 + (c_3^i)^2} \quad \text{Eq. (2.16)}$$

$$f_b = \frac{2c_2^i |z_2 - z_1|^2}{(z_1 + z_2) \bar{u}(z_1, z_2)} \quad \text{Eq. (2.17)}$$

The co-coherence can be calculated using Equation 2.18, which was later suggested by IEC 61400-1 (2005).

$$\gamma_u(f, d_z) = \exp \left\{ -12 \left[ \sqrt{\frac{f d_z}{\bar{u}_{hub}}} + \left( 0.12 \frac{d_z}{8.1 L_c} \right)^2 \right] \right\} \quad \text{Eq. (2.18)}$$

$$\left\{ \begin{array}{l} 0.7^z, \quad z \leq 60m, \quad L^c = \quad 42m, \quad z \geq 60m. \end{array} \right.$$

# CHAPTER 3

## 3 METHODOLOGY

### 3.1 Site Description

Five 500k wind turbines make up the Bockstigen offshore wind farm, which was built three kilometres off the SW coast of Gotland Island in the Baltic. The initiative was sparked by a desire to learn more about bottom-mounted offshore wind turbine installations, and more specifically, about driving monopiles into rock-core strata.

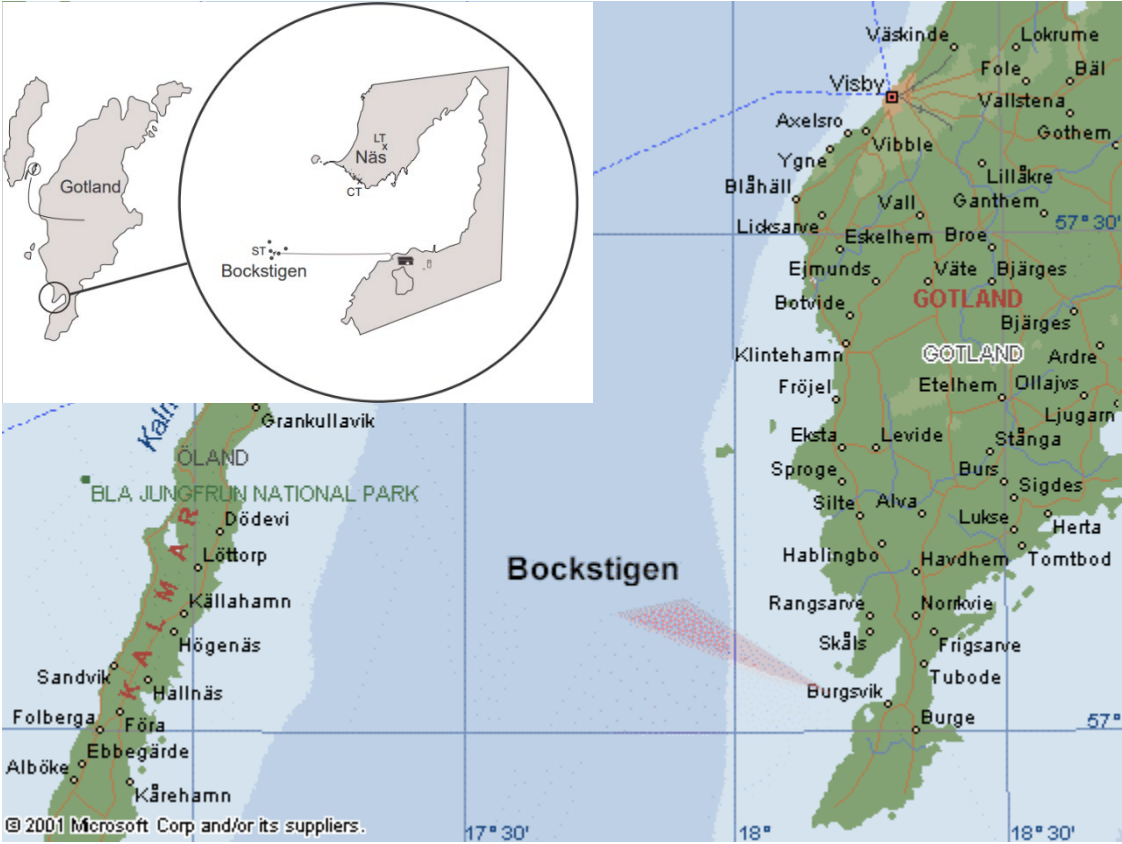
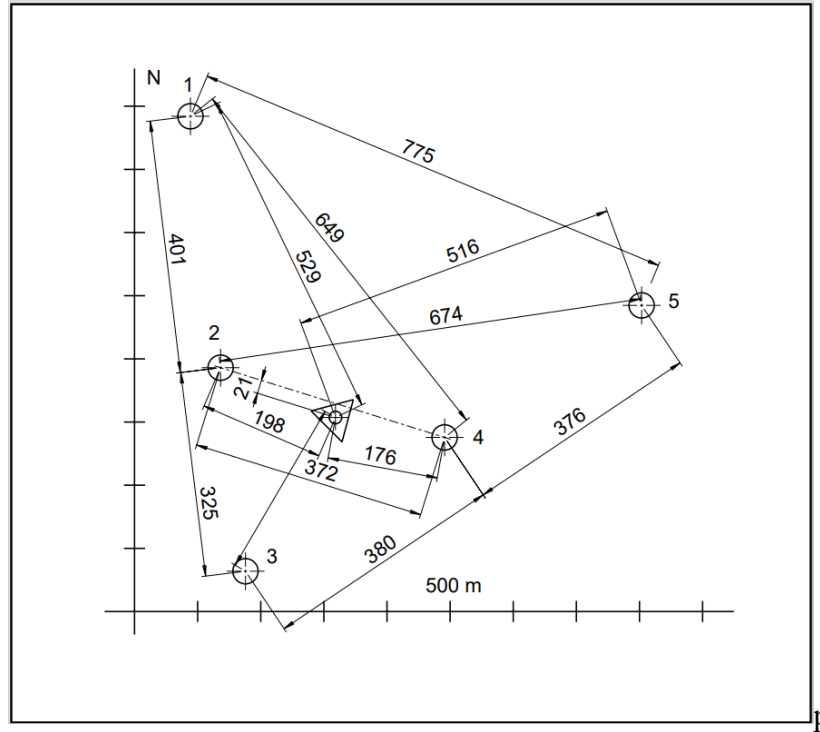


Figure 3-1: The Bockstigen wind farm situated in Sweden (Source: Hansen, 2005)

One meteorological mast and one instrumented turbine are used for the observations, but no data from the rotating system itself is considered. Multiple data loggers were used to sample the data (20 Hz data scan), and the resulting signals are transferred via optical fibre cable (4.5 km) to a

shoreside cottage. There are five wind turbines and a mast at this location. At a typical wind speed of 8m/s, annual energy production fluctuates between 1420 MWh and 1539 MWh (Goran, 2005).



*Figure 3-2: Orientation of meteorological mast and wind turbines*

The individual turbines are located in a V-formation 350m apart in an area with a water depth varying between 5.5 and 6.5m. On each of the turbines the various instrumentation types carried out through the Bockstigen available channels includes, the tower bending moment in the x and y directions, tower torsion, tower shear force in the x and y directions, linear acceleration in the x, y, z directions, angular acceleration in the x, y, z directions, wind speed, temperature, relative humidity, and active power.

Table 2: Summary of wind speed measurements

<b>Year</b>	<b>2000-2001</b>
<b>Terrain</b>	Offshore
<b>Orography</b>	Flat
<b>Number of Masts</b>	1
<b>Height [s]</b>	40 m
<b>Wind Speed measurements at 5 heights</b>	8, 22, 37 and 40 m
<b>Wind direction measurements at 3</b>	8, 22 and 37
<b>Frequency</b>	1 Hz
<b>Hours of measurements</b>	1239
<b>Number of runs</b>	1239

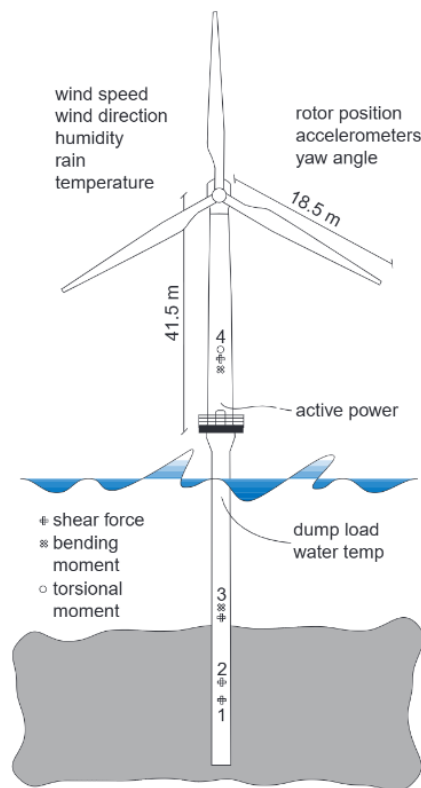


Figure 3-3: Position of Sensor on Wind Turbine 4 (Source: Goran Ronsten)

### 3.2 Bockstigen observation data information

The raw time series of wind speed and wind direction observations from a 50-meter offshore mast in Bockstigen, Gotland, Sweden, are included in this collection. Since the year 2000, the period comprises roughly 1,200 hours of offshore measurements.

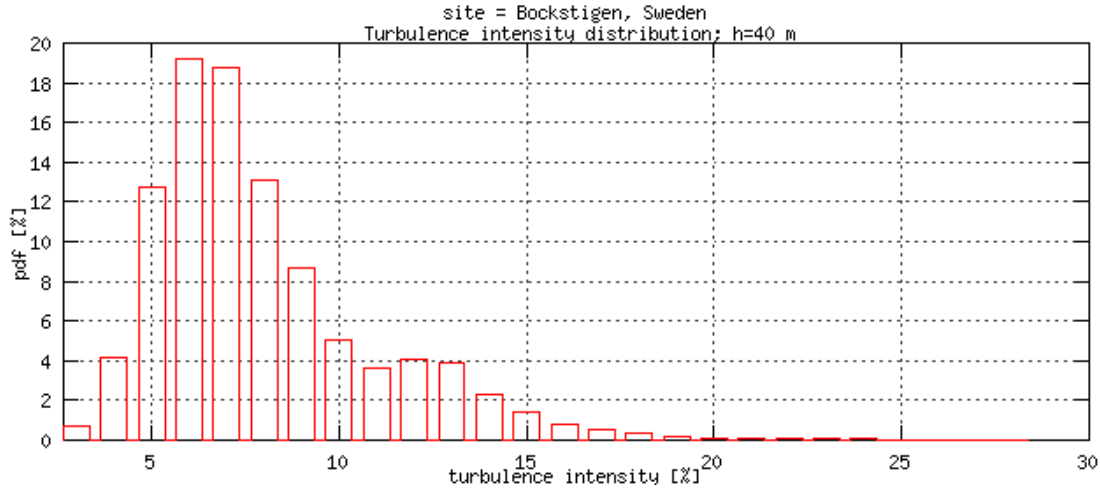


Figure 3-4: Nominal Turbulence Distribution (Source: Goran Ronsten)

### 3.3 Data Processing

The procedure to carry on the data processing of the data is provided in Appendix A. The main statistical quantities of interest are: (i) the mean wind speed data; (ii) the variance; and (iii) the standard deviation.

#### 3.3.1 Categorization of the time series.

According to Patil et al., (2022), the time series is considered stationary when the absolute relative difference between the moving mean and the static mean does not exceed 20%, and 40%. The cutoff values are calculated using the Lumley and Panof, 1964-proposed statistical uncertainty associated with the variance of a random process relative to its mean.

Applying the MOST model to the data would allow us to estimate the distribution of the non-dimensional stability parameter ( $\zeta$ ) as a function of the mean wind speed ( $\bar{u}$ ), and recognize stability conditions such as non-neutral (i.e., where  $|\zeta| > 0.1$ ) and strongly unstable or stable stratifications ( $|\zeta| > 0.5$ ). The co-coherence and quad-coherence (the imaginary part of the root coherence) between the vertical velocity component  $w$  and the velocity of the wave surface  $= d/dt$  will be used to investigate the interactions between wind turbulence and the sea surface.

#### 3.3.2 Mean

The mean of each column was computed using the equation Eq. 3.1. The mean wind speed is the average of the given set of numbers and is calculated by dividing the sum of given numbers by the total number of numbers.

$$A = \frac{1}{n} \sum_{i=2}^n a_i \quad (\text{Eq. 3.1})$$

Where  $A$  is the Arithmetic mean,  $n$  is the number of values or observations and  $a_i$  is the wind speed data.

### 3.3.3 Variance and Standard Deviation:

The variance of each column,  $s$ , was computed using the equation given in Eq. 3.2. The variance is a measure of dispersion of the data, meaning it is a measure of how far a data set is spread out from their average value.

$$s_2 = \frac{\sum(x_1 - \bar{x})^2}{n - 1} \quad (\text{Eq. 3.2})$$

In the above equation,  $x_i$  is the value of one observation,  $\bar{x}$  is the mean wind speed of all observation data and  $n$  is the sample size.

The standard deviation of the wind speed data was computed using the Eq. 3.3. The standard deviation is a statistic that measures the dispersion of a dataset relative to its mean and is calculated as the square root of the variance. A low standard deviation indicates that the values tend to be close to the mean of the set, while a high standard deviation indicates that the values are spread out over a wider range.

$$\sigma = \sqrt{\frac{\sum(x_1 - \bar{x})^2}{n - 1}} \quad (\text{Eq. 3.3})$$

where  $\sigma$  is the standard deviation.

### 3.3.4 Max and Min Wind Speed

The extreme values of the data are recorded. The wind speed blowing at different height was then extracted and grouped according to the direction which has the most prominent wind considering at different heights and direction.

### 3.3.5 Stationarity test:

In addition, a stationarity test was performed on the data. For each of the wind speed calculated and recorded, a stationarity test was performed using the RA function in MATLAB, while in the reality most of the stochastic process are non-stationary due to their randomness in nature, very often time-series measurements assume the data as stationary. The mean, variance, and auto-correlation structure do not alter over time in a stationary process. Although stationarity can be precisely defined mathematically, for our purposes, we refer to a series that appears flat, has no trend, has constant variance over time, has a consistent autocorrelation structure across time, and does not exhibit periodic fluctuations. If the time series is not stationary, one of the following methods can usually make it stationary.

1. We can difference the data. That is, given the series  $Z_t$ , we create the new series:

$$Y_t = z_t - z_{t-1}$$

There will be one extra data point in the original set than in the differenced set. The data can be changed multiple times, although usually only one time is sufficient.

2. If there is a trend in the data, the residuals from the fit can be modeled. Straight-line fittings and other simple ones are widely used. The primary focus of the fit is to remove the long-term trend.
3. If the variance is not constant, you can stabilize it by taking the logarithm of the series or the square root of the series. If any of the input values are negative, a suitable constant must be added before the transformation is applied. The fitted (or expected) values are then derived by subtracting this constant from the model to obtain the anticipated values and projections for future points.

The stationarity test revealed that the wind speed is constant. This because, the measurement was made in the winter, when the wind is more likely to be unstable and turbulent than in the spring. The nonstationary series was subsequently subjected to a detrending function, which resulted in the series being stationary.

As seen Figure 3-5 and 3-6 of the wind speed and wind direction are shown at different height i.e. 8m, 22m, 37m, 40m.

where the blue wind speed shows the non-stationary series and the red show it when stationary, after it has been detrended



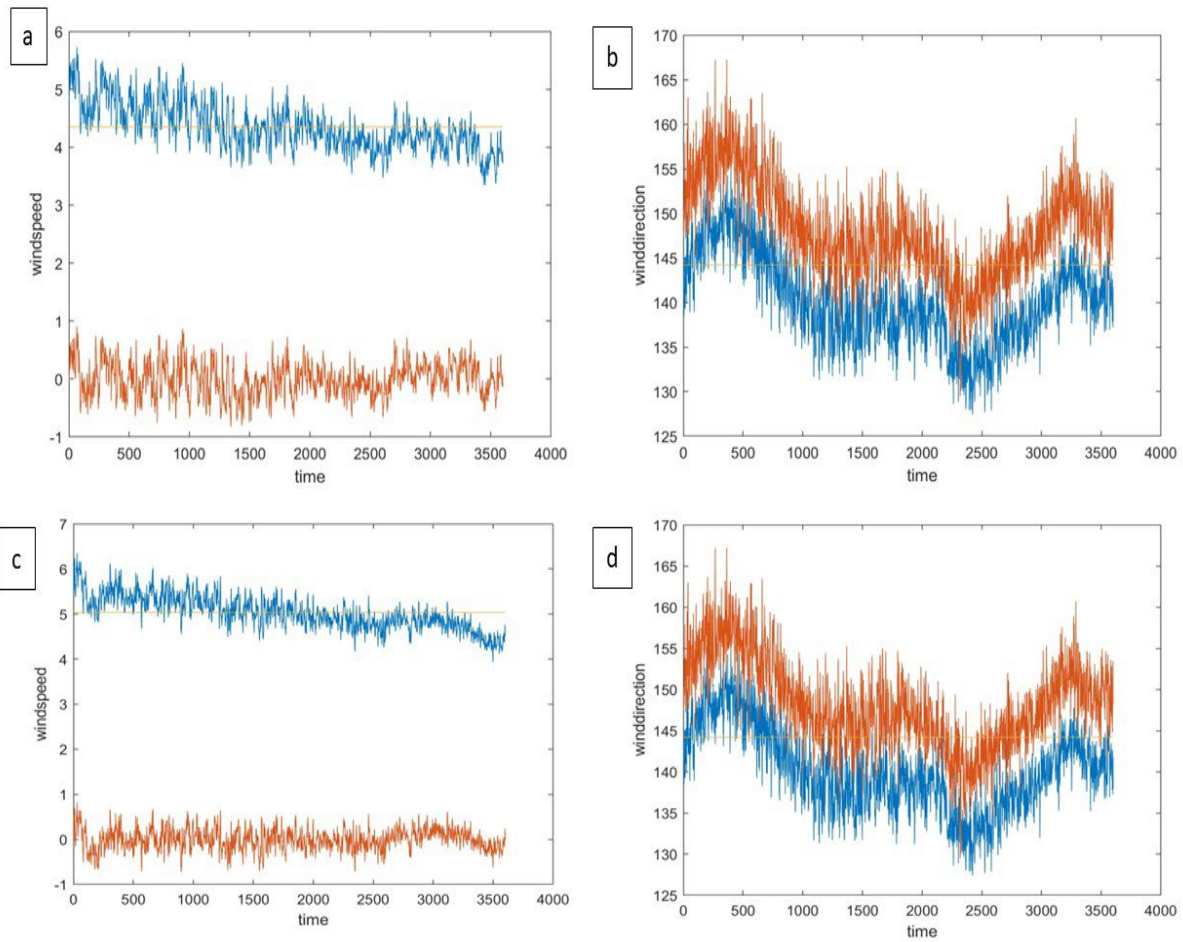


Figure 3-5: (a: wind speed at 8m elevation; (b) wind direction at 8m elevation; (c) wind speed at 22m elevation; (d) wind direction at 22m elevation

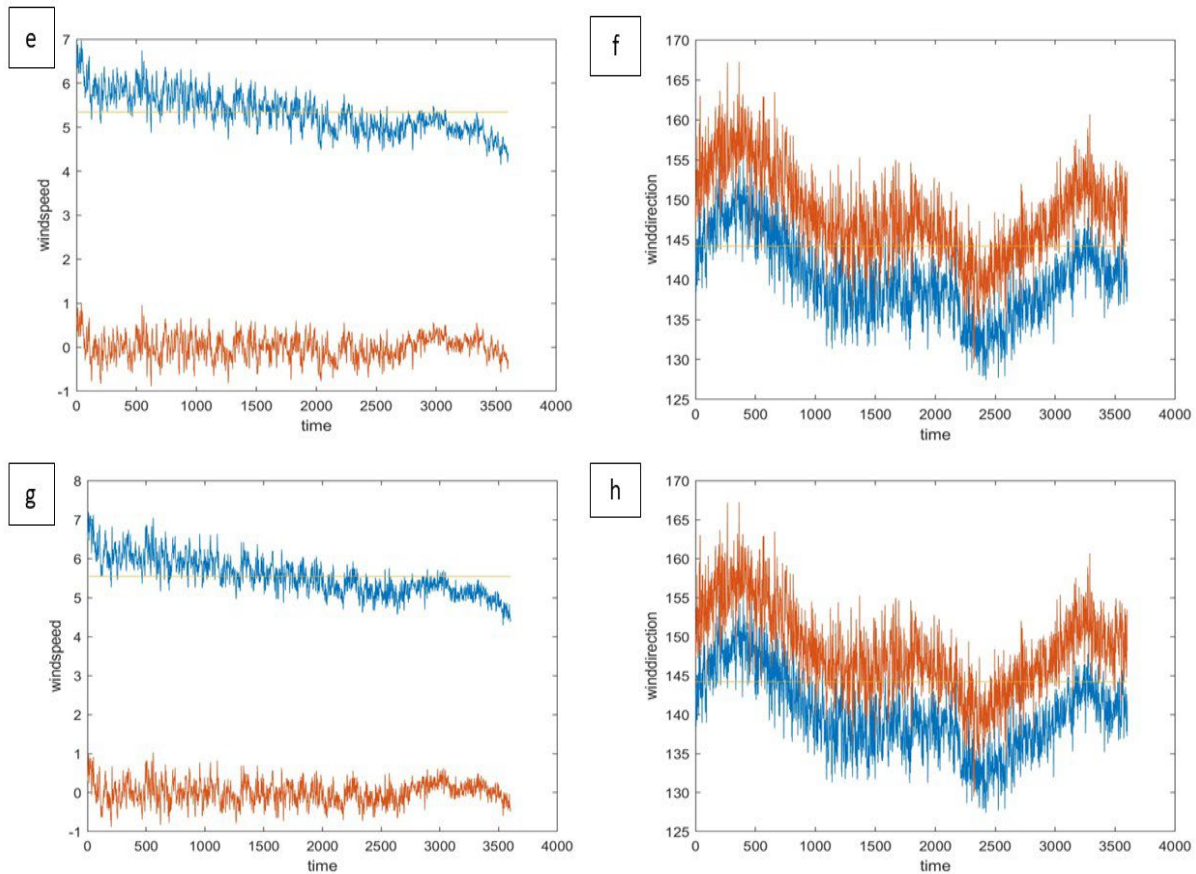


Figure 3-6 (e: wind speed at 37m elevation; (f) wind direction at 37m elevation; (g) wind speed at 40m elevation; (h) wind direction at 40m elevation

### 3.4 Power Spectra Density Using Welch vs FFT Method

The power spectral density (PSD) is commonly used to evaluate the power levels of the frequency components that are present in a signal. The PSD spectra is an essential representation of power vs frequency relationship of a time series data. The PSD indicates the range of power at which the signal frequencies are functioning and details the power of various frequencies included in the signal.

In this study we are comparing the spectra density of the data measured and we use two different method Welch and Fast Fourier Transform (FFT) to compare and show in a plot at different height.

#### 3.4.1.1 Welch Method

The method relies on periodogram spectrum estimates, which are generated via a time-to-frequency transformation of a signal. The Welch spectrum uses a Hanning function to divide the

signal into discrete bands. Welch's segment count is relative to the overlap size and segment length. The degree of freedom (DOF) is traditionally employed to assess the statistical stability of the welch spectra. For instance, in the study of ocean wave statistics, a degree of freedom (DOF) of at least 16 is adequate. By default, MATLAB's Welch technique for estimating power spectral density uses the longest feasible signal segments to get 8 segments with at most 50% overlap. A Hamming window is applied to each individual section. The PSD estimate is calculated by taking the mean of the adjusted periodograms.

#### **3.4.1.2 Fast Fourier Transform (FFT)**

In the fast fourier transform (FFT), the signal is converted from the time to the frequency domain. The built-in Matlab function `fft()` determines the signal's fft value. The PSD explains the frequency-dependent power (or variance) distribution of the time series. The PSD displays the energy variation as a function of frequency. In other words, the PSD reveals where there are significant frequency differences and where there are minor variations. The FFT approach is used to calculate the PSD directly, or the autocorrelation function can be computed first and then converted.

# Chapter 4

## 4 RESULTS and DISCUSSION

### 4.1 Data description, Quality Assessment, and Numerical Simulations

Here, statistical analysis are performed on the dataset to spot trends, outliers, and anomalies. In line with the approach taken by Patil et al., 2022, we would compute the moving mean and the moving standard deviation of the along-wind components across a 10-minute window to evaluate the first- and second-order stationarity of the velocity records.

#### 4.1.1 Turbulence spectra

The Power Spectral Density (PSD) of the velocity variations is critical for describing the wind-induced reaction of wind turbines. Separate estimations will be done for the along-wind, crosswind, and vertical-wind components to determine the PSD of the Bockstigen wind farm as a function of the lowered frequency  $f_r$  for various stability classes. Patil et al. (2022) employed a technique to normalize PSDs based on the friction velocity ( $u^*$ ) and the non-dimensional turbulent kinetic energy dissipation rate ( $\epsilon$ ). Different heights above mean sea level (a.m.s.l.) might likewise be used to compare the estimated spectra.

In the figures, the power levels of the frequency components that are present in a signal are specified by the PSD. The PSD, which details the power of various frequencies included in the signal allows us to discover the range of power at which the signal frequencies are functioning. As observed in the figures, the PSD profile is essentially a representation of power vs frequency.

The spectra density of the data measured is analysed using two different methods: the Welch and Fast Fourier Transform (FFT). A comparison between the power spectra at different heights obtained from each one of the two methods is carried on.

When evaluating the power spectra density of time series data, the Welch method is a viable alternative. By averaging or smoothing out the periodogram estimations, the method was created to cut down on periodogram variance. The Welch method is a refined version of the Bartlett method (insert ref.). The Welch method allows the overlapping of the data, and each data segment is windowed prior to computation of the PSD. At the fundamental level, the Welch's method divides the original signal in several pieces, therefore increasing the size of the sample and averages the spectra of increased signal.

The figure below shows that the dominant wind speed is between wind directions are between 223–350° at Bockstigen. The increasing wind speed to the left indicates that winds come primarily from the west, but also the north and the east.

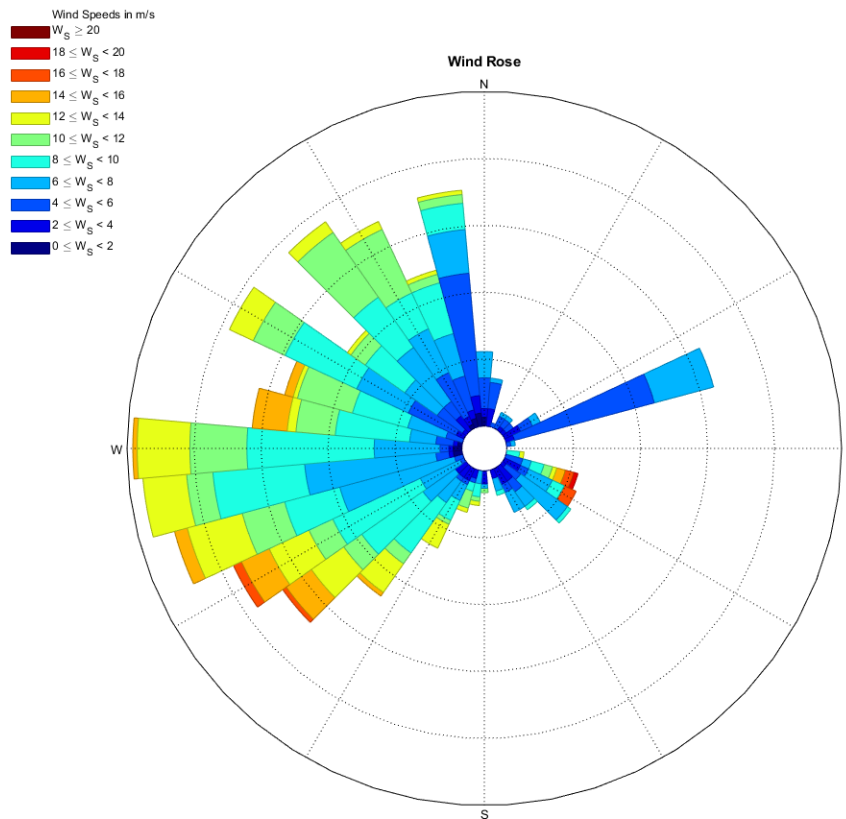


Figure 4-1: Windrose: distribution of stability of wind speed

Figure 4-2 plots the frequency distribution of the wind speeds. According to the frequency distribution of the wind speed, a large occurrence frequency is observed for wind speeds between 6 and 10 m/s. The distribution of the mean wind speed as a function of the Richardson number is plotted in Figure 4-3 for the different anemometer heights. As observed, the mean wind speed was larger at the 9 m a.m.s.l., which is associated with a Richardson number between -0.2 to 0.4 and -1.2 and 1.0. For the remaining anemometer height, the mean wind speed was significantly smaller than at 9 m a.m.s.l.

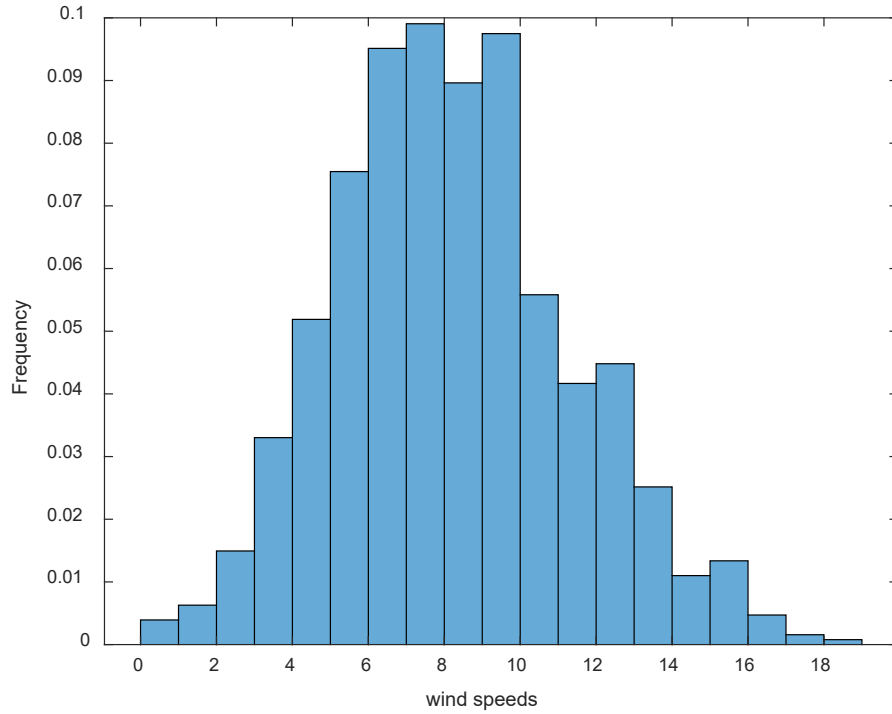


Figure 4-2: Frequency distribution of wind speed

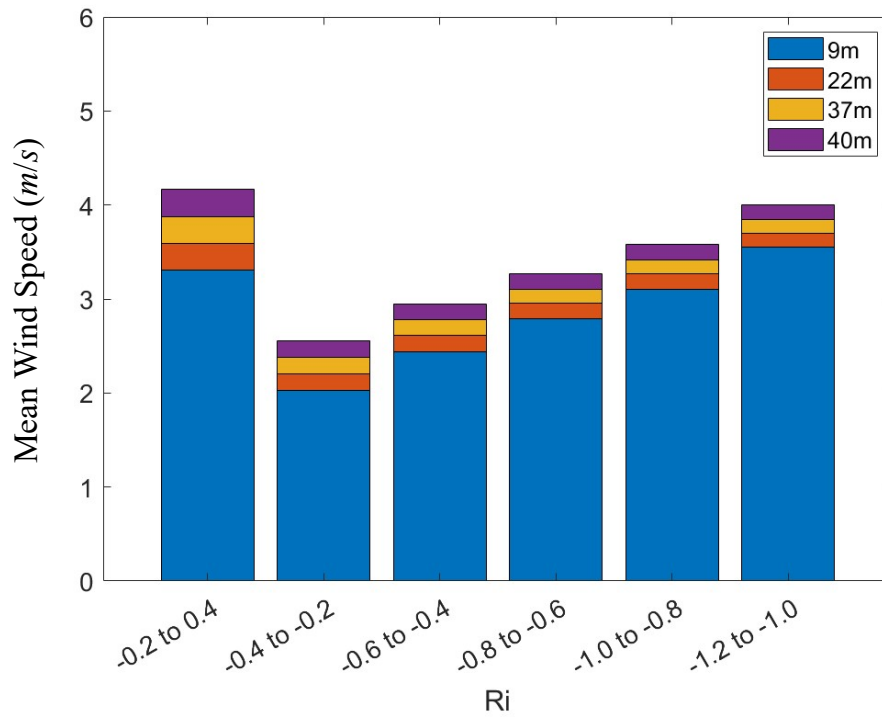


Figure 4-3: Mean Wind speed distribution as a function of the Richardson number

Welch and FFT PSD estimations were calculated using the MATLAB code provided in Appendix A. The Welch and FFT PSDs are drastically different from one another, as shown in Figures 4.4 and 4.13 which is due to the sensitivity of the FFT signal to non-stationarity. For signals that have non-stationary components, the FFT offers a more accurate estimate than the Welch. The Fast Fourier Transform (FFT) is used to obtain a global spectrum estimate of the signal, although it is very susceptible to noise and other non-stationary effects. Since you are averaging a succession of FFTs produced on each segment, the frequency resolution of the Welch spectrum is lower than that of a single FFT. FFT spectral analysis of the time series signal showed no peak in the spectrum as a function of wind speed, as depicted in the images. According to (Shah and Ferziger 1997), these findings are characteristic of turbulent flows, which feature repetitive structures that differ in size, strength, and frequency.

The Welch and the FFT spectra matched in the in the higher frequency range of the velocity spectra, from frequency  $f$  above  $10^{-2}$  Hz, but in the lower frequency range the Welch spectra exceeded the FFT spectra.

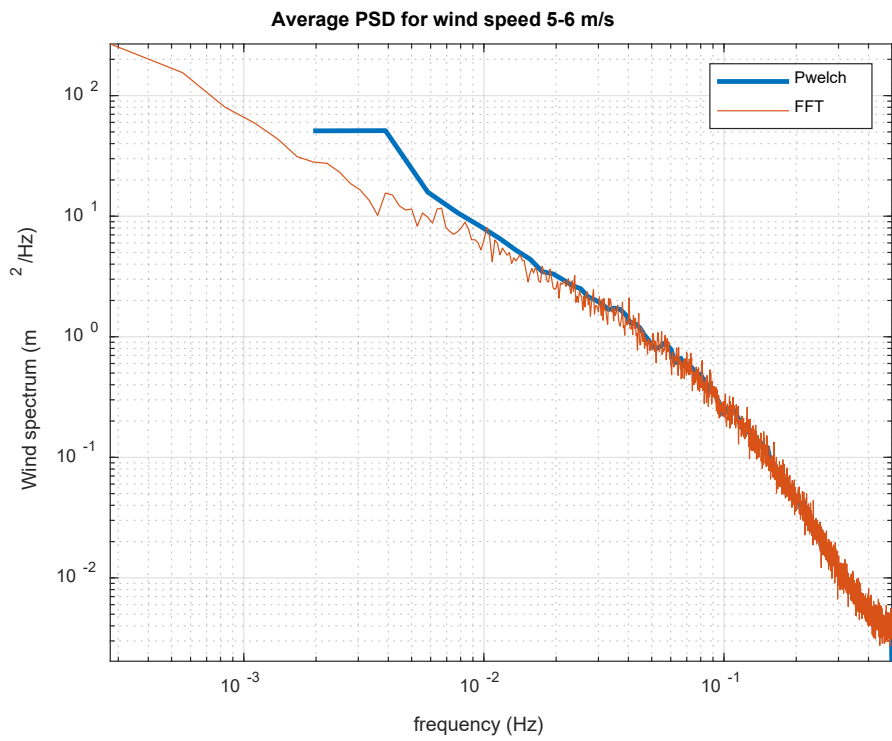


Figure 4-4: Average PSD for wind speed 5-6 m/s

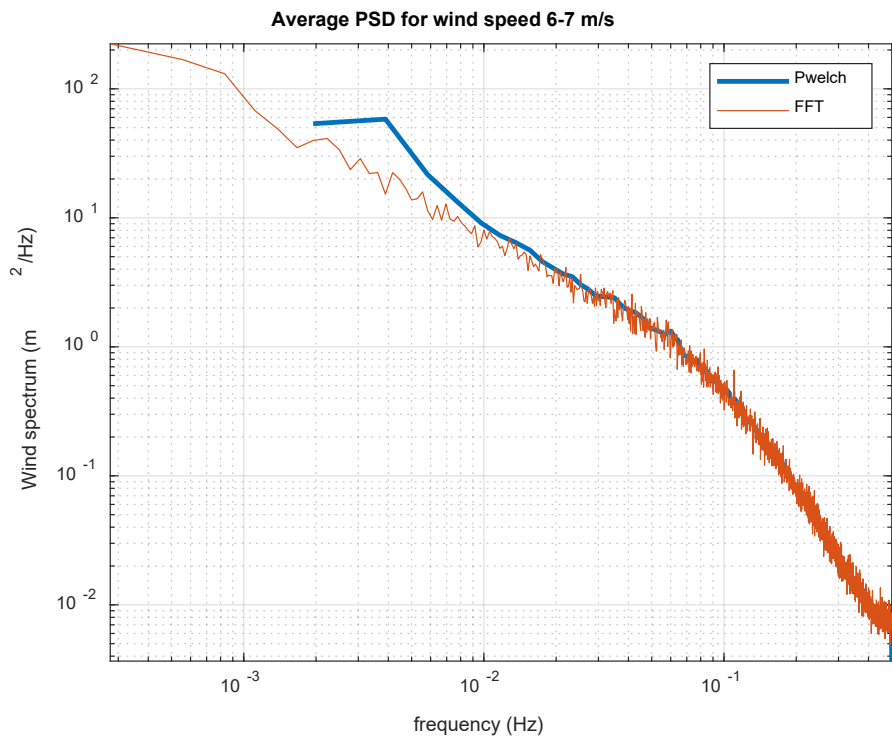


Figure 4-5: Average PSD for wind speed 6-7 m/s



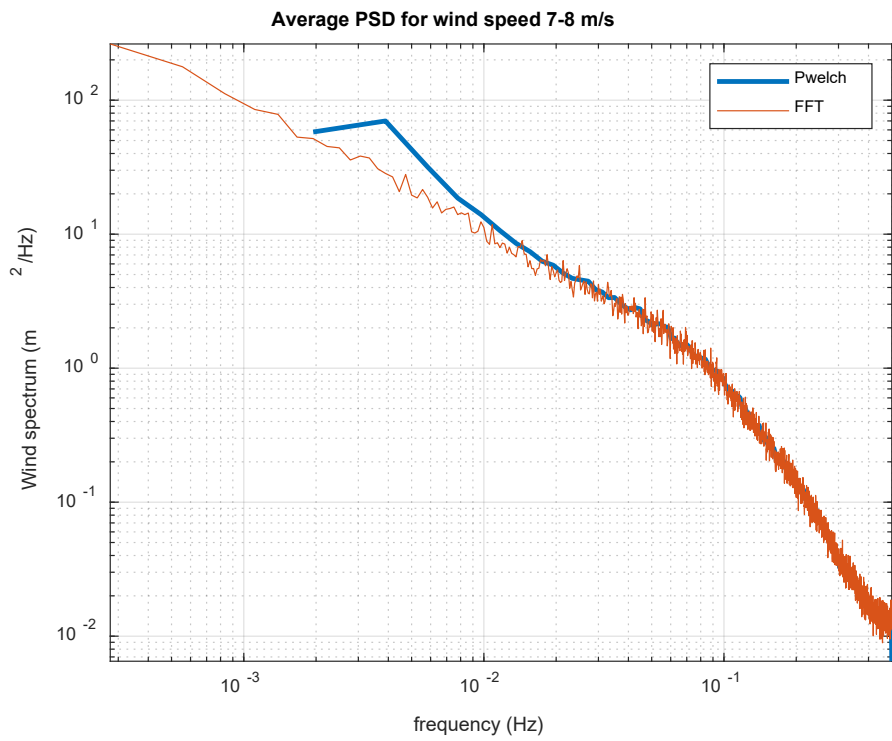


Figure 4-6: Average PSD for wind speed 7-8 m/s

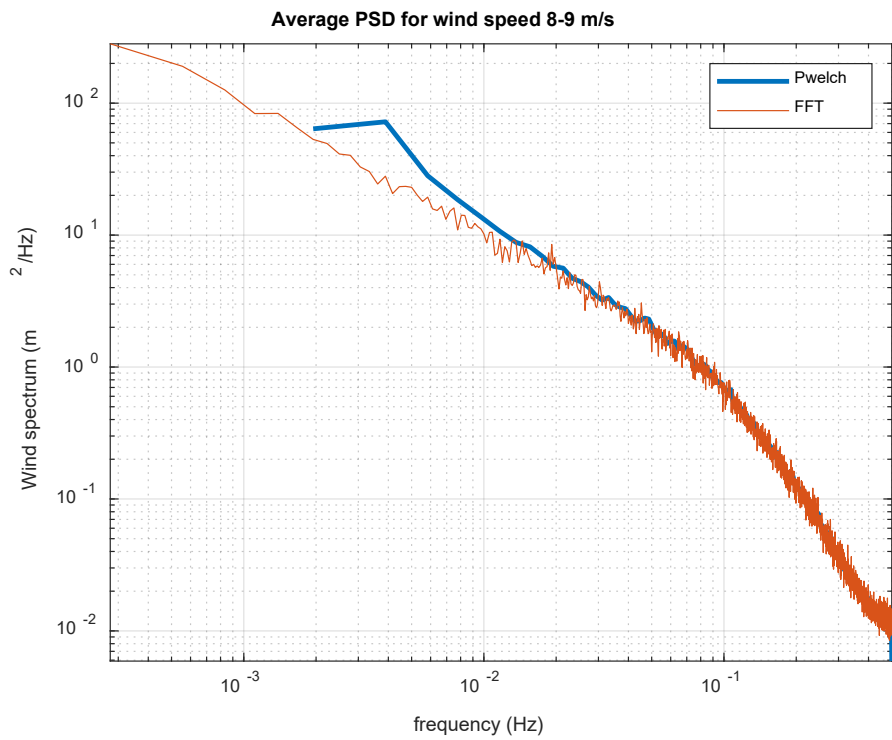


Figure 4-7: Average PSD for wind speed 8-9 m/s

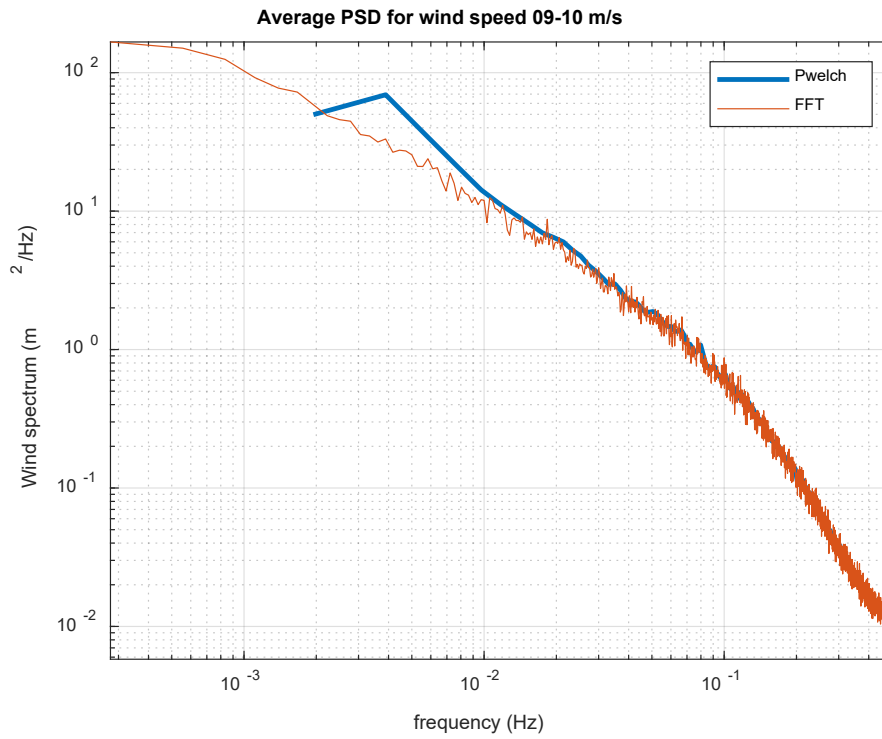


Figure 4-8: Average PSD for wind speed 9-10 m/s

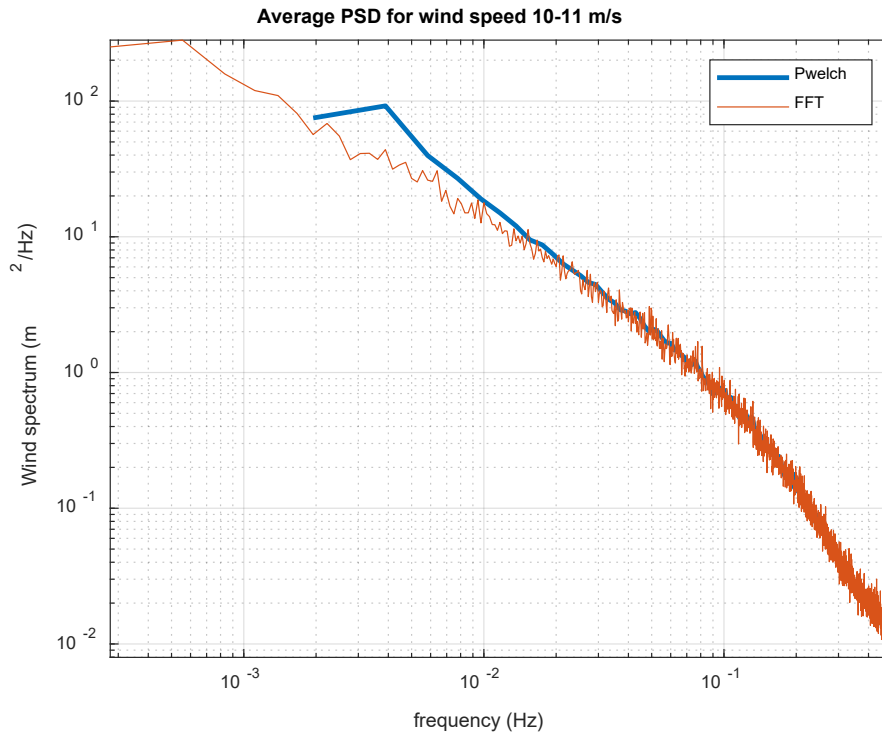


Figure 4-9: Average PSD for wind speed 10-11 m/s

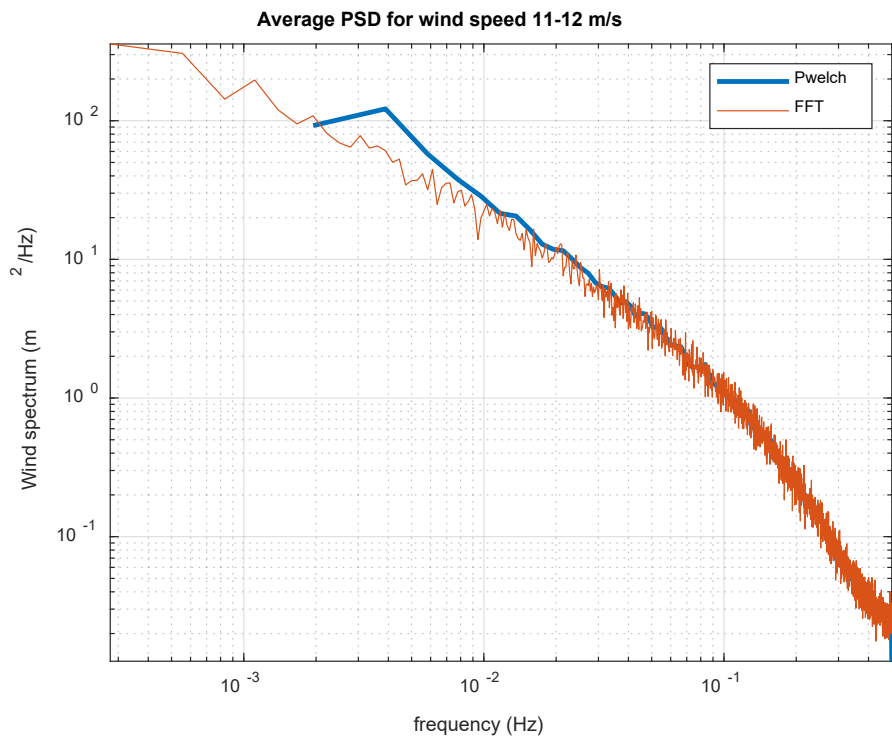


Figure 4-10: Average PSD for wind speed 11-12 m/s

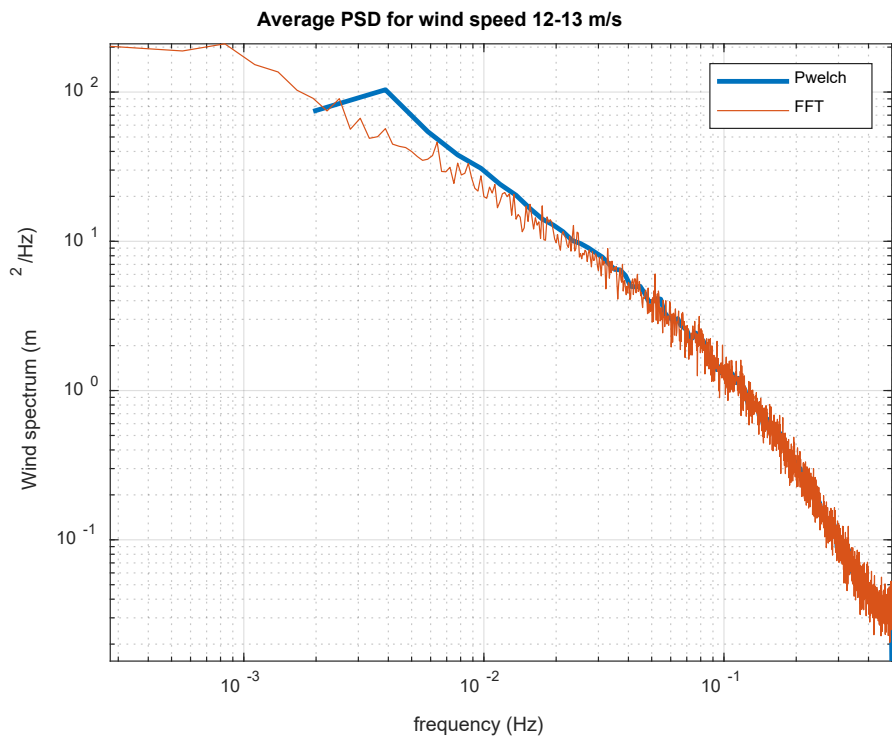


Figure 4-11: Average PSD for wind speed 12-13 m/s

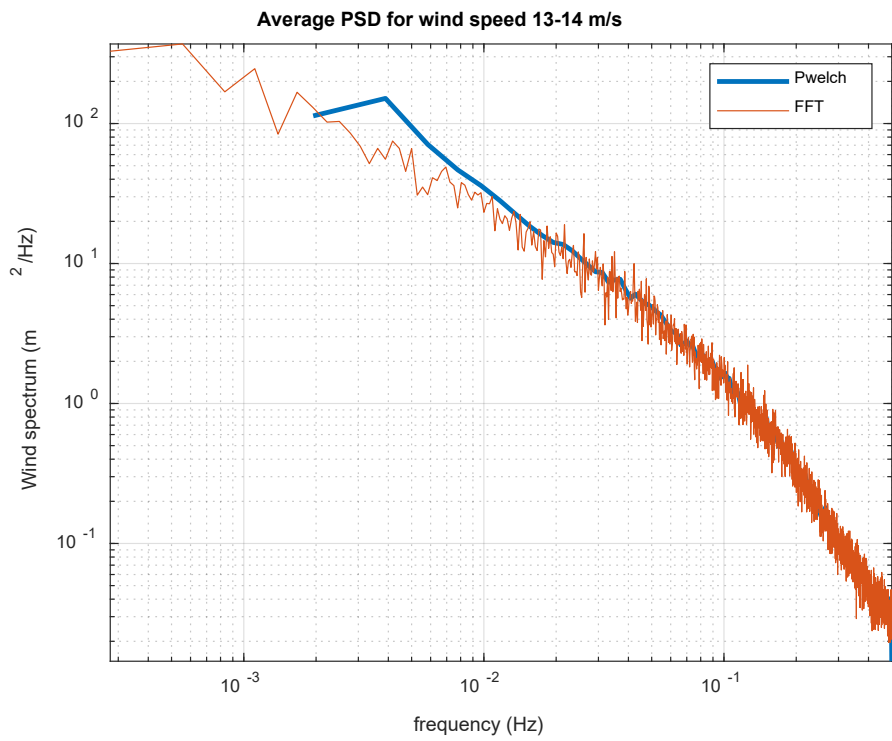


Figure 4-12: Average PSD for wind speed 13-14 m/s

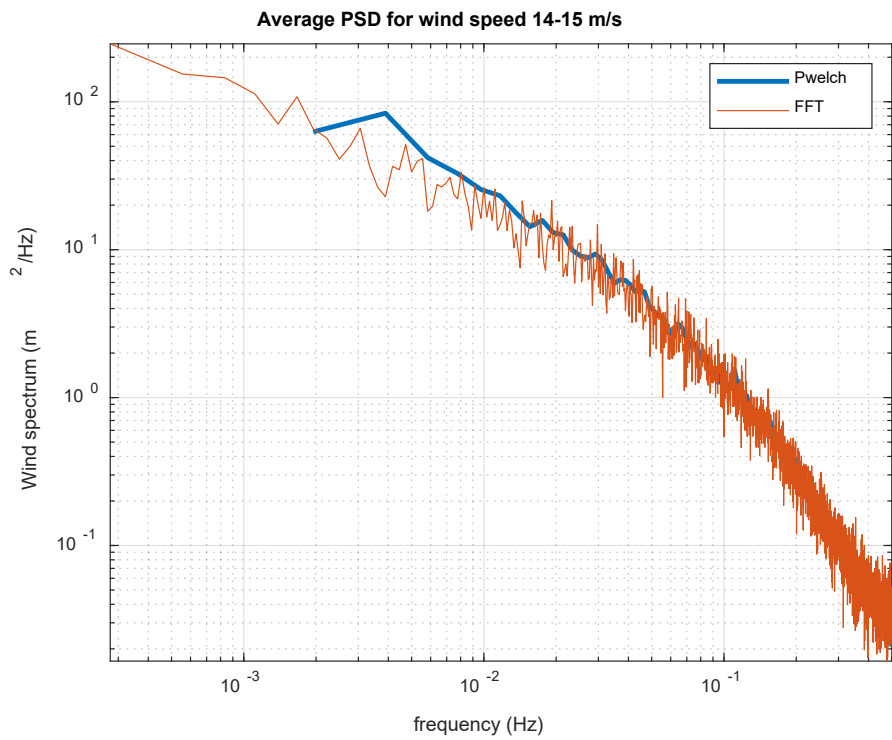


Figure 4-13: Average PSD for wind speed 14-15 m/s

Figure.4-14 to Figure 4-17 plots the non-dimensional velocity spectra versus the reduced frequency at different anemometer heights:  $z = 9, 22.5, 37,$  and  $40 \text{ m}$ , for different stability conditions. As observed in the figures, the maximum value of the non-dimensional spectra estimated at  $9 \text{ m a.m.s.l.}$  is close to unity for the neutral stability conditions, as observed by Putri et al and described by Kaiman et al. (1972), but achieves a maximum of nearly  $0.85,$  and  $0.35$  for the unstable and stable conditions, respectively. The maximum value of the non-dimensional spectra exceeded unity for the unstable condition estimated at  $22.5, 37,$  and  $40 \text{ m a.m.s.l.},$  and for the neutral condition for the spectra estimated at  $37,$  and  $40 \text{ m a.m.s.l.}$  For the stable condition, the non-dimensional spectra reached a maximum value of nearly  $0.4,$  estimated at  $37 \text{ m a.m.s.l.}$

Except for  $z = 40 \text{ a.m.s.l.},$  the difference in the normalized spectra at high frequencies for the three different stability conditions is negligible.

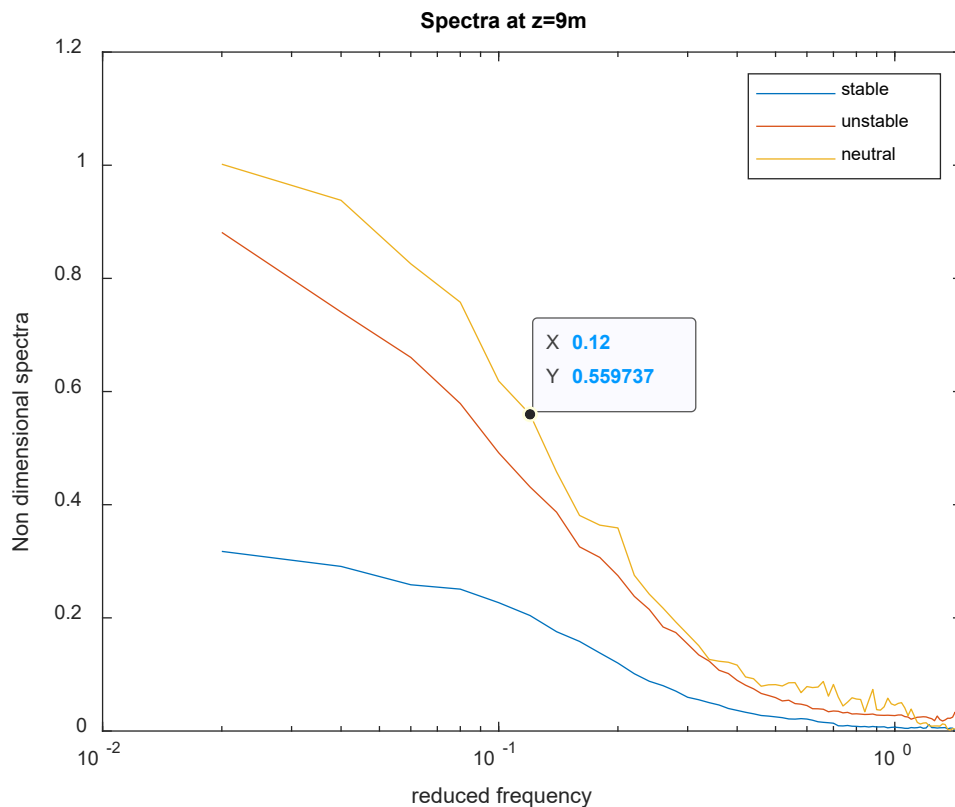


Figure.4-14: Average spectra at  $9\text{m}$  @ 3 conditions

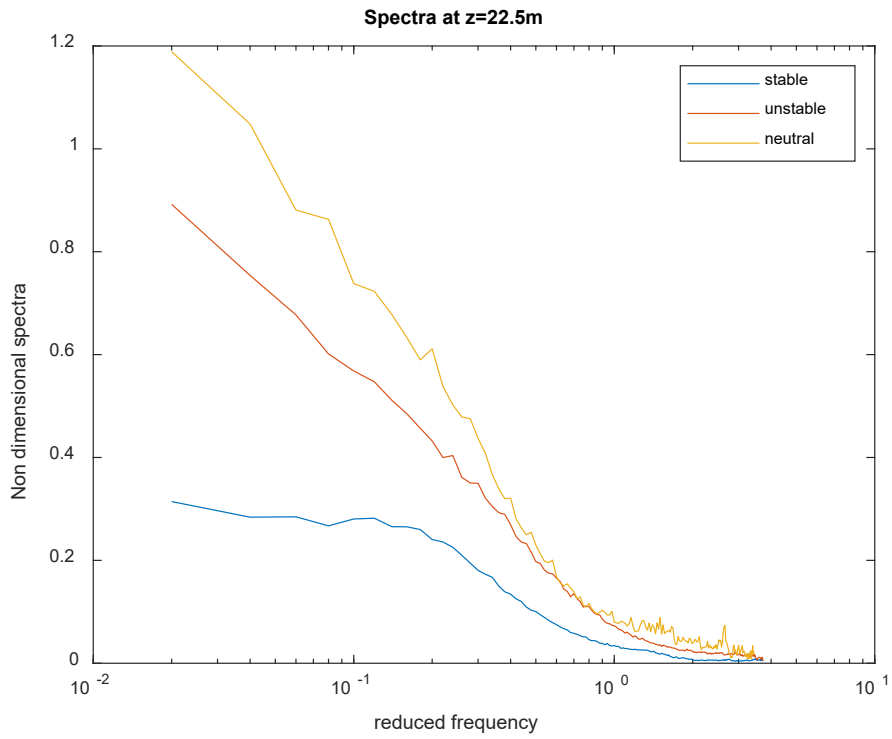


Figure 4-15: Average spectra at 22.5m @ 3 conditions

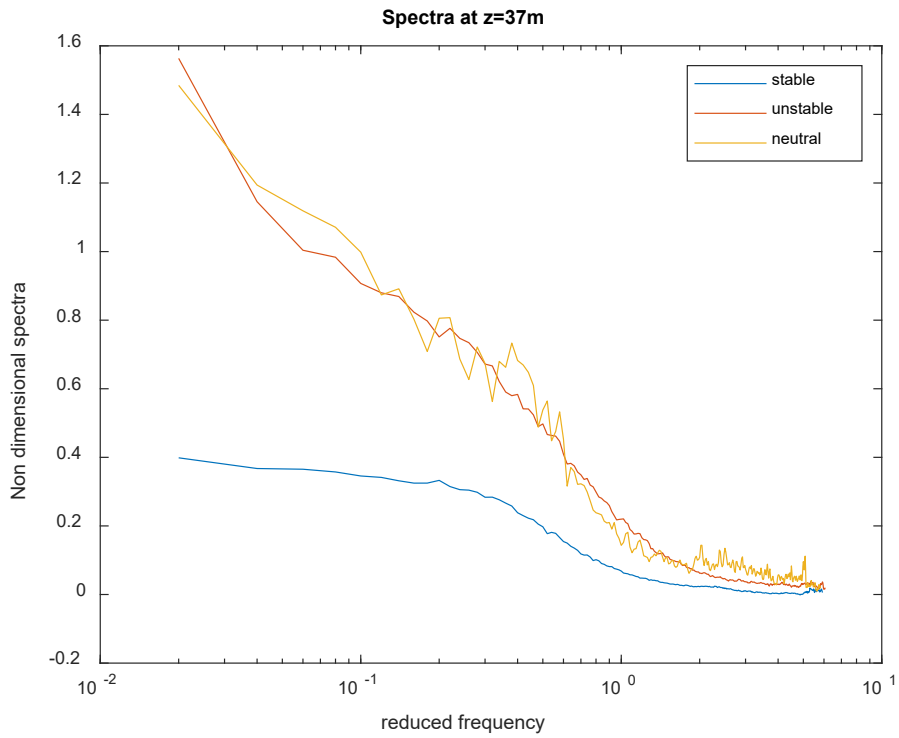
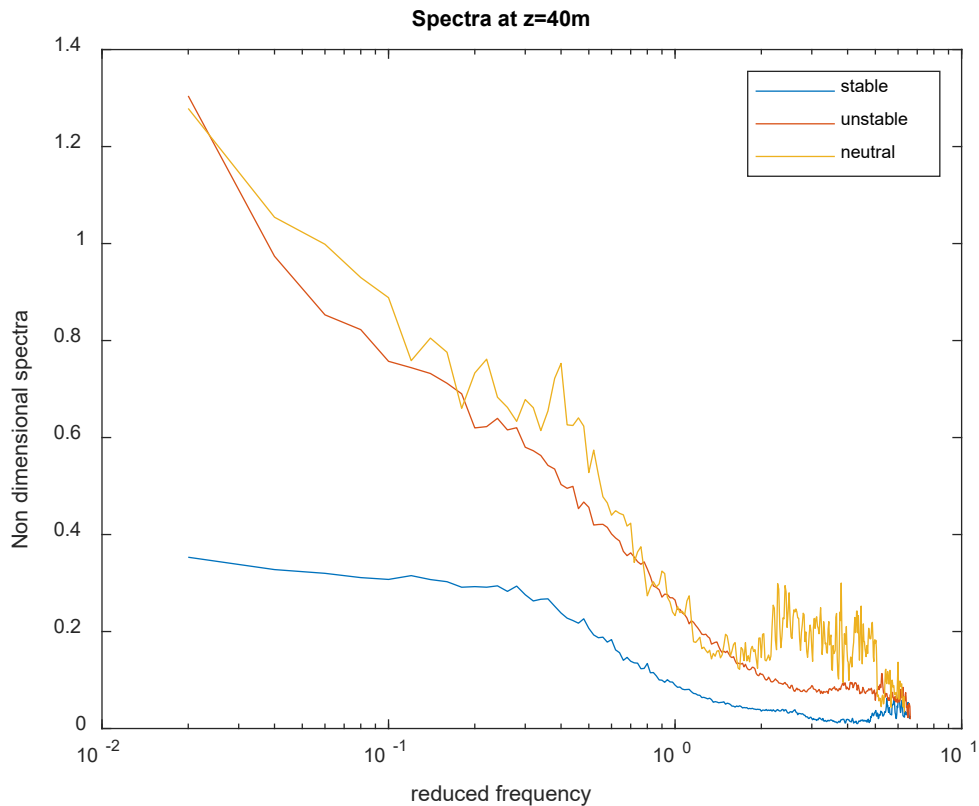


Figure 4-16: Average spectra at 37 m @ 3 conditions



*Figure 4-17: Average spectra at 40 m @ 3 conditions*

From Figure 4.18 through Figure 4.20, you can see the estimated spectra for the anemometers at 9, 22.5, 37, and 40 m a.m.s.l. in steady conditions. Under steady conditions, as seen in the images, the spectral gap appears to shift toward lower frequencies as altitude is reduced above the surface. For steady conditions, the non-dimensional spectra peaked at 37 m a.m.s.l., increasing to values close to 0.4 at low frequencies, while they dipped to their lowest at 22.5 m a.m.s.l., approaching values near to 0.33.

Similarly, for the unstable and neutral conditions, the maximum value of the non-dimensional spectra occurred at the height of 37 m a.m.s.l., growing close to 1.6 for the unstable condition and exceeding 1.5 for the neutral conditions. The minimum value of the non-dimensional spectra occurred at the height of 9 m a.m.s.l., reaching a value close to 0.9.

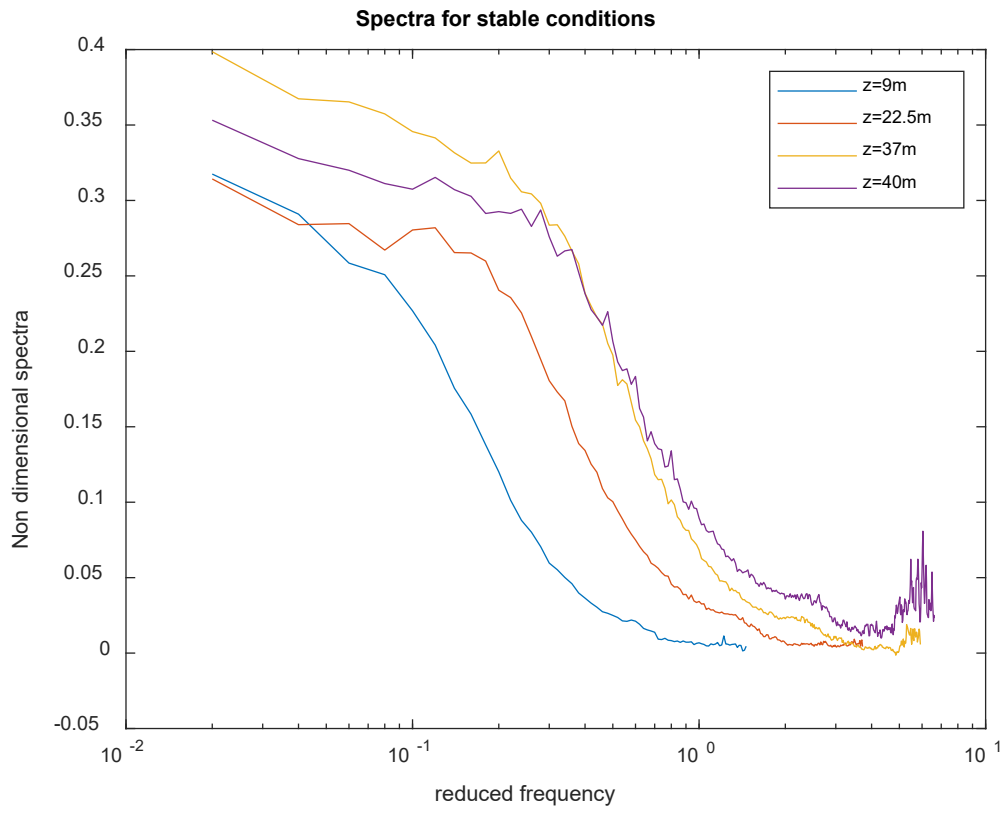


Figure 4-18: Average spectra 1 conditions @ 4 heights



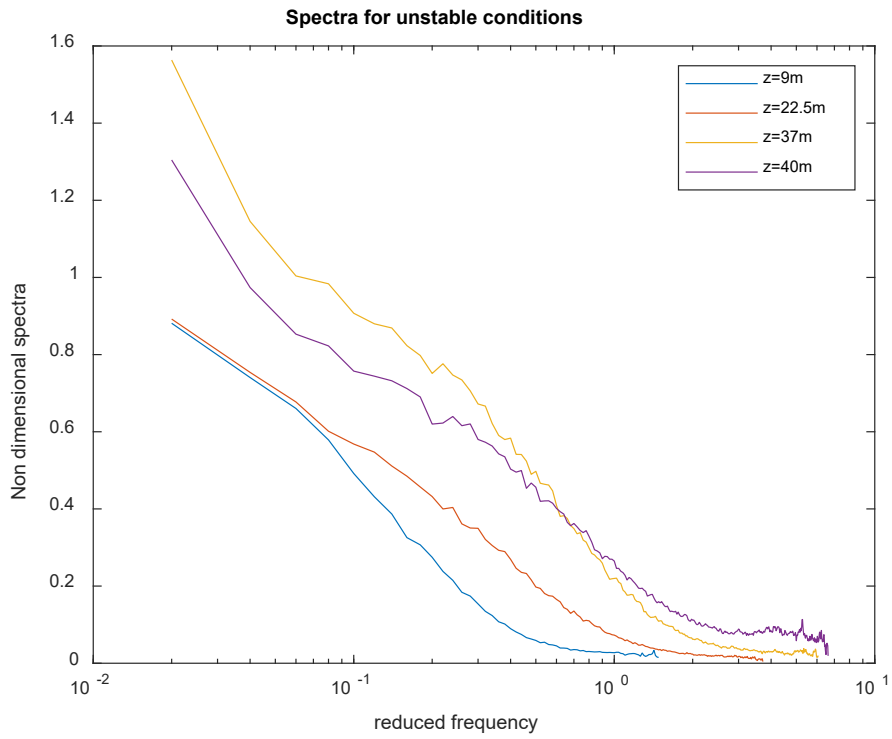


Figure 4-19: Average spectra unstable condition @ 4 heights

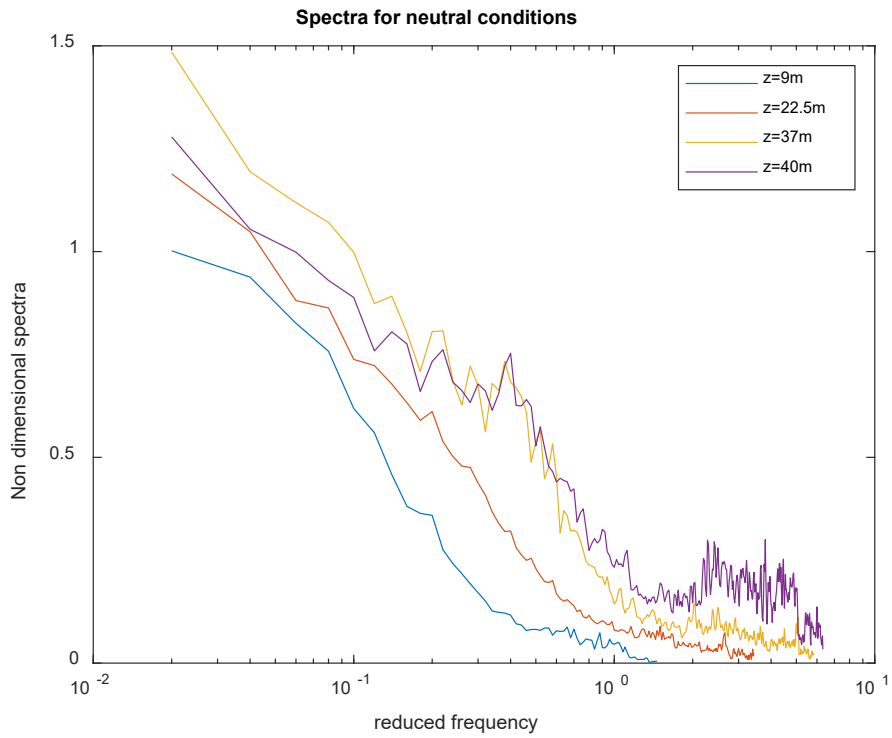


Figure 4-20: Average spectra Neutral condition @ 4 heights

### 4.1.2 Coherence of turbulence

At varying separation distances relative to measurement heights, we examine the along-wind co-coherence estimations. Large, wind-sensitive structures have been modelled using the co-coherence since the 1960s. The co-coherence estimates were computed using the Welsh's method.

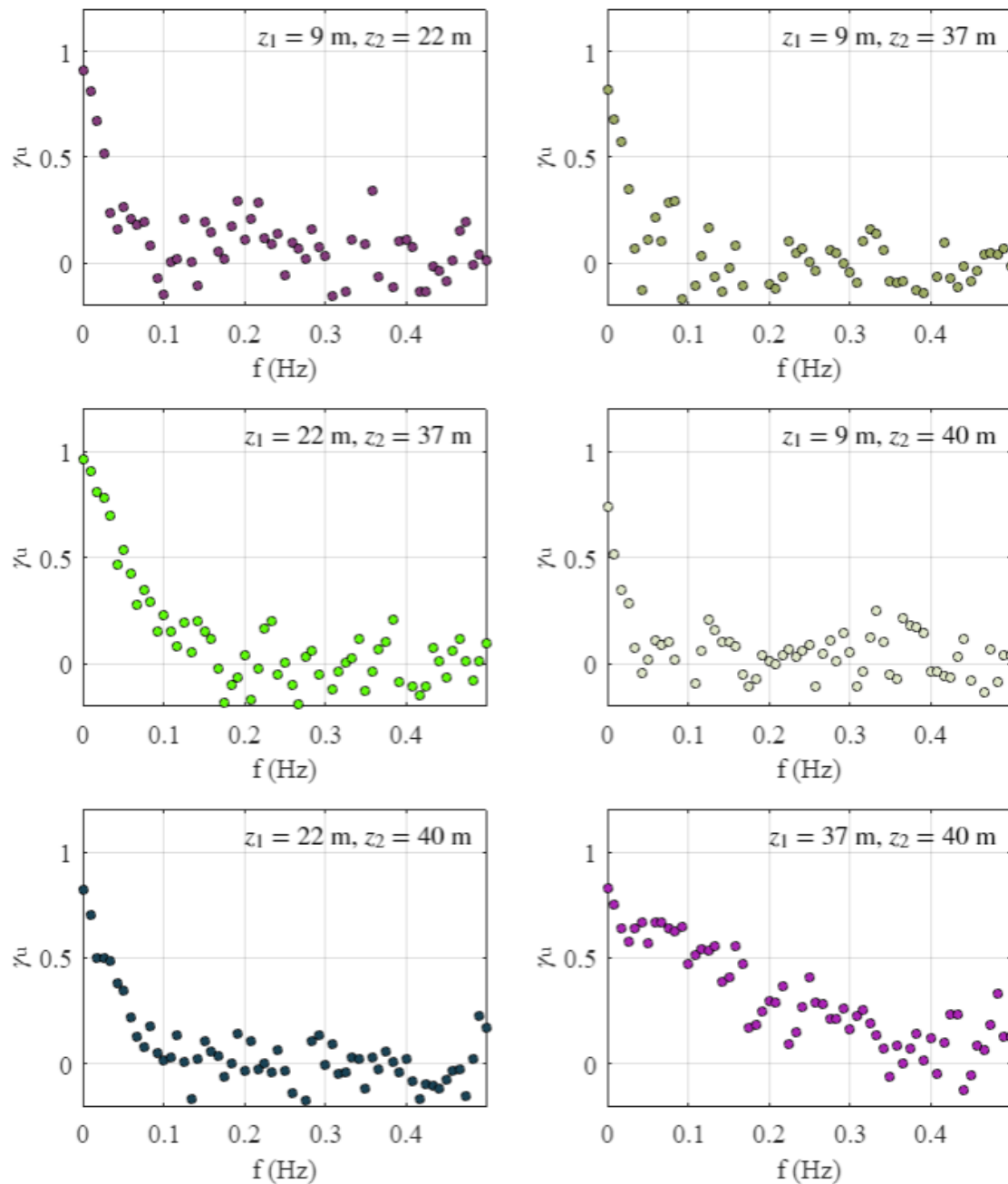


Figure 4-21: Co-coherences of the along-wind velocity components at four different vertical separation distances.

Eight segments and 50% overlap was used to avoid statistical uncertainty.

The computation of the coherence data was computed using the MATLAB code provided in Appendix B. The coherence data was computed from the mean wind speed data of all the wind speed time series. The function “getDistance” (Appendix B), was used to help to speed up the computation of the co-coherence of turbulence by avoiding redundant pairs of sensors. This process gets the distance  $d$  between two locations and the associated indices of the unique pairs of sensors. In the sequence, the average wind speeds at height were computed. To estimate the coherence, the function “cohence.m” (Appendix B) was employed. The function uses the MATLAB predefined function “cpsd” which estimates the cross power spectral density (CPSD) of two discrete-time signals,  $x$  and  $y$ , using Welch’s averaged, modified periodogram method of spectral estimation.

The co-coherence of the along-wind, denoted by  $\gamma_u$ , for longitudinal separation versus non-dimensional frequency is shown in Figure 4-21. The co-coherence estimates are presented for four separation distances  $dz$  because four measurement heights ( $z_1 = 9$  m,  $z_2 = 22$  m,  $z_3 = 37$  m, and  $z_4 = 40$  m) were used. As observed by Putri et al. (2022) for the Vindeby dataset, and predicted by the predictive equations, the co-coherence plots for the Bockstigen dataset show large decay at small frequency for all the different vertical separations. In fact, the co-coherence decreased rapidly for all the separations, except the separation between 37 and 40 m a.m.s.l. For the vertical separation between 37 and 40 m a.m.s.l, the co-coherence died out slower. Unlike the other separations, the negative co-coherence was relatively small.

# Chapter 5

## 5 CONCLUSIONS and RECOMMENDATIONS

In this analysis, we analyse wind records from the Bockstigen offshore mast to determine the spectrum properties of turbulence. The objectives of this research were to (i) study the characteristics of turbulent wind spectra offshore, (ii) to investigate the features of offshore turbulence in the frequency domain using the Bockstigen wind speed data. (iii) to quantify and compare the observations and similarities between the co-coherence characteristics of offshore turbulence obtained from Bockstigen wind data at various heights.

The main conclusions are listed as follows:

- i. Understanding the primary distinctions between the PSDs derived by the Welch and FFT methods was the first step in the research project. It is interesting to note that the spectrum of the time series signal did not exhibit a peak in the PSD. This was the case irrespective of the wind speed as well as the method that was employed to compute the PSD. Both the Welch and the FFT spectra were identical in the higher frequency range of the spectrum, beginning at a frequency of  $f$  that was greater than  $10^{-2}$  Hz; however, the Welch spectra were superior to the FFT spectra in the lower frequency range.
- ii. The peak value for the non-dimensional velocity spectra was larger for the neutral stability conditions (with the maximum value reaching unity), followed by the unstable and stable condition, respectively. In addition, the difference in the normalized spectra at high frequencies was negligible, regardless of the stability condition.
- iii. The co-coherence decreased rapidly at small frequency for all the different vertical separations, except the separation between 37 and 40 m a.m.s.l, in which the co-coherence died out slower. There was negative co-coherence for all the vertical separations, for the separations where large decay of the co-coherence was observed. For the separation between 37 and 40 m a.m.s.l, the negative co-coherence was small.

For wind turbine design, the study of the co-coherence at lateral separations is required. This is not covered in this study due to the availability of data and as such is categorised under future works and recommendations. The Bocktigen co-coherence of turbulence could be compared with

relevant standard models as showcased by Putri et al., (2022), however this has not been considered in this work and could be further researched on.

## 6 References

1. IEC 61400-3, International Electrotechnical Commission. (2019). Wind energy generation systems-Part 1: Design requirements. International Electrotechnical Commission: Geneva, Switzerland
2. IEC 61400-1, Wind Turbines — Part 1: Design Requirements (third ed.) (2005) Geneva (Switzerland): [https://webstore.iec.ch/preview/info\\_iec61400-1%7Bed3.0%7Den.pdf](https://webstore.iec.ch/preview/info_iec61400-1%7Bed3.0%7Den.pdf)
3. Kaimal, J. C., Wyngaard, J. C., Izumi, Y., & Coté, O. R. (1972). Spectral characteristics of surface-layer turbulence. *Quarterly Journal of the Royal Meteorological Society*, 98(417), 563–589. <https://doi.org/10.1002/qj.49709841707>
4. Elgendi, M., AlMallahi, M., Abdelkhalig, A., & Selim, M. Y. (2023). A review of wind turbines in complex terrain. *International Journal of Thermofluids*, 100289.
5. Tasneem, Z., Al Noman, A., Das, S. K., Saha, D. K., Islam, M. R., Ali, M. F., ... & Alam, F. (2020). An analytical review on the evaluation of wind resource and wind turbine for urban application: Prospect and challenges. *Developments in the Built Environment*, 4, 100033.
6. *How The Wind Turbine Works* . (n.d.). Retrieved July 22, 2023, from <https://www.energy.gov/eere/wind/how-wind-turbine-works-text-version>
7. Mann, J. (1994). The spatial structure of neutral atmospheric surface-layer turbulence. *Journal of Fluid Mechanics*, 273, 141-168. doi:10.1017/S0022112094001886
8. von Kármán, T. (1948). Progress in the statistical theory of turbulence. *Proceedings of the National Academy of Sciences*, 34(11), 530–539. <https://doi.org/10.1073/pnas.34.11.530>
9. Hansen, Kurt Schaldemose; Vasiljevic, Nikola; Sørensen, Steen Arne (2021). Turbulence measurements from the Bockstigen mast and offshore wind farm. Technical University of Denmark. Dataset. <https://doi.org/10.11583/DTU.15028272.v1>
10. Cheynet, E., Jakobsen, J. B., & Obhrai, C. (2017). Spectral characteristics of surface-layer turbulence in the North Sea. *Energy Procedia*, 137, 414-427
11. ISO19901, J. E. (2015). Petroleum and Natural Gas Industries. Specific Requirements for Offshore Structures. Part 1: Metocean Design and Operating Considerations.
12. API, R. (2). SK (2005):“Design and Analysis of Station keeping Systems for Floating Structures”
13. N. O. R. S. O. K. (2007). Actions and action effects. Edition, 2, 36-57.

14. DNV, G. (2019). Coupled analysis of floating wind turbines. Recommend Practice DNVGL-RP-0286.
15. Veritas, N. (2000). Environmental conditions and environmental loads. Oslo, Norway: Det Norske Veritas.
16. Veritas, N. (2021). Floating wind turbine structures. Det Norske Veritas.
17. Andersen, O. J., & Løvseth, J. (2006). The Frøya database and maritime boundary layer wind description. *Marine Structures*, 19(2-3), 173-192.
18. Taylor, A., Anthony, K. C., Harris, R. I., Berrman, P. W., Wootton, L. R., Scruton, C., ... & Shears, M. (1971). *The Modern Design of Wind-Sensitive Structures*.
19. Andersen, O. J., & Løvseth, J. (2006). The Frøya database and maritime boundary layer wind description. *Marine Structures*, 19(2-3), 173-192.
20. Cheng, E. D. H., & Chiu, A. N. L. (1990). An expert system for extreme wind simulation. *Journal of Wind Engineering and Industrial Aerodynamics*, 36, 1235–1243. [https://doi.org/10.1016/0167-6105\(90\)90120-2](https://doi.org/10.1016/0167-6105(90)90120-2)
21. Ochi, M. K., & Shin, V. S. (1988, May). Wind turbulent spectra for design consideration of offshore structures. In *Offshore technology conference*. OnePetro.
22. Shiotani, M. (1975). Turbulence measurements at the sea coast during high winds. *Journal of the Meteorological Society of Japan*. Ser. II, 53(5), 340–354. [https://doi.org/10.2151/jmsj1965.53.5\\_340](https://doi.org/10.2151/jmsj1965.53.5_340)
23. J.A.B. Wills, A. Grant, C.F. Boyack. *Offshore Mean Wind Profile* (1986) London (UK): <https://trid.trb.org/view/428217>
24. RP-0286 coupled analysis of floating wind turbines. DNV. (2019). Retrieved April 10, 2023, from <https://www.dnv.com/energy/standards-guidelines/dnv-rp-0286-coupled-analysis-of-floating-wind-turbines.html>
25. Argyle, P., Watson, S., Montavon, C., Jones, I., & Smith, M. (2018). Modelling turbulence intensity within a large offshore wind farm. *Wind Energy*, 21(12), 1329–1343. <https://doi.org/10.1002/we.2257>
26. Calif, & Emilion. (2012). Characterization and stochastic modeling of wind speed sequences. *Springer Proceedings in Physics*, 235–238. [https://doi.org/10.1007/978-3-642-28968-2\\_50](https://doi.org/10.1007/978-3-642-28968-2_50)

27. Stevens, R. J. A. M., & Meneveau, C. (2017). Flow structure and turbulence in wind farms. *Annual Review of Fluid Mechanics*, 49(1), 311–339. <https://doi.org/10.1146/annurev-fluid-010816-060206>
28. Brand, A. J., & Wagenaar, J. W. (2012). Turbulent wind turbine wakes in a wind farm. *Springer Proceedings in Physics*, 231–234. [https://doi.org/10.1007/978-3-642-28968-2\\_49](https://doi.org/10.1007/978-3-642-28968-2_49)
29. Larsen, G. C. (2009). A simple stationary semi-analytical wake model. Retrieved April 9, 2023, from [https://backend.orbit.dtu.dk/ws/portalfiles/portal/122941920/Simple\\_analytical\\_wake\\_model\\_final\\_10.pdf](https://backend.orbit.dtu.dk/ws/portalfiles/portal/122941920/Simple_analytical_wake_model_final_10.pdf)
30. Chamorro, L. P., Arndt, R. E., & Sotiropoulos, F. (2011). Turbulent flow properties around a staggered wind farm. *Boundary-Layer Meteorology*, 141(3), 349–367. <https://doi.org/10.1007/s10546-011-9649-6>
31. Göçmen, T., & Giebel, G. (2016). Estimation of turbulence intensity using rotor effective wind speed in Lillgrund and horns rev-I offshore wind farms. *Renewable Energy*, 99, 524–532. <https://doi.org/10.1016/j.renene.2016.07.038>
32. Andersen, S. J., Sørensen, J. N., Mikkelsen, R., & Ivanell, S. (2016). Statistics of les simulations of large wind farms. *Journal of Physics: Conference Series*, 753, 032002. <https://doi.org/10.1088/1742-6596/753/3/032002>
33. Madsen HAa, Thomsen K, Larsen GC. A new method for prediction of detailed wake loads. In *Proceedings of IEA Joint Action of Wind Turbines 16th Symposium*. Thor S-E (ed.). Boulder, USA, May 2003 at NREL, 2003; 171–188.
34. Madsen HAa, Larsen GC, Larsen TJ, Troldborg N, Mikkelsen R. Calibration and validation of the dynamic wake meandering model implemented in the aeroelastic code HAWC2. *Journal of Solar Energy Engineering* 2010; 132: 041014 (14 pages).
35. Larsen GC, Madsen HAa, Thomsen K, Larsen TJ. Wake meandering—a pragmatic approach. *Wind Energy* 2008; 11: 377–395.
36. Frandsen ST. Turbulence and turbulence-generated structural loading in wind turbine clusters. Risø-R-1188(EN). Risø National Laboratory, Technical University of Denmark: Roskilde, Denmark, 2007.
37. Ainslie JF. Calculating the flow field in the wake of wind turbines. *Journal of Wind Engineering and Industrial Aerodynamics* 1988; 27: 213–224.



38. Ainslie JF. Wake modelling and the prediction of turbulence properties. In Proceedings of the 8th British Wind energy Association Conference, Cambridge, 19-21 March 1986; 115–120.
39. Keck RE, Veldkamp D, Madsen HAa, Larsen GC. Implementation of a mixing length turbulence formulation into the dynamic wake meandering model. *Journal of Solar Energy Engineering* 2011; 134: 021012 (13 pages).
40. Madsen HAa, Larsen GC, Thomsen K. Wake flow characteristics in low ambient turbulence conditions. In Proceedings of Copenhagen Offshore Wind 2005, 2005.
41. Keck RE, de Mare M, Churchfield MJ, Lee S, Larsen G, Madsen HAa. Two improvements to the dynamic wake meandering model: including the effects of atmospheric shear on wake turbulence and incorporating turbulence build up in a row of wind turbines. Submitted to *Journal of Wind Energy* July 2012.
42. Barthelmie RJ, Hansen K, Frandsen ST, Rathmann O, Schepers JG, Schlez W, Phillips J, Rados K, Zervos A, Politis ES, Chaviaropoulos PK. Modelling and measuring flow and wind turbine wakes in large wind farms offshore. *Wind Energy* 2009; 12: 431–444. DOI: 10.1002/we.348
43. Keck, R.-E., de Maré, M., Churchfield, M. J., Lee, S., Larsen, G., & Aagaard Madsen, H. (2013). On atmospheric stability in the dynamic wake meandering model. *Wind Energy*, 17(11), 1689–1710. <https://doi.org/10.1002/we.1662>
44. Putri, R. M., Obhrai, C., & Knight, J. M. (2019). Offshore wind turbine loads and motions in unstable atmospheric conditions. *Journal of Physics: Conference Series*, 1356(1), 012016. <https://doi.org/10.1088/1742-6596/1356/1/012016>
45. Breton, S.-P., Nilsson, K., Olivares-Espinosa, H., Masson, C., Dufresne, L., & Ivanell, S. (2014). Study of the influence of imposed turbulence on the asymptotic wake deficit in a very long line of wind turbines. *Renewable Energy*, 70, 153–163. <https://doi.org/10.1016/j.renene.2014.05.009>
46. Goit, J. P., & Meyers, J. (2015). Optimal control of energy extraction in wind-farm boundary layers. *Journal of Fluid Mechanics*, 768, 5–50. <https://doi.org/10.1017/jfm.2015.70>
47. Anderson, W., Passalacqua, P., Porté-Agel, F., & Meneveau, C. (2012). Large-eddy simulation of atmospheric boundary-layer flow over fluvial-like landscapes using a

- dynamic roughness model. *Boundary-Layer Meteorology*, 144(2), 263–286.  
<https://doi.org/10.1007/s10546-012-9722-9>
48. APA Porté-Agel, F., Wu, Y.-T., Lu, H., & Conzemius, R. J. (2011). Large-eddy simulation of atmospheric boundary layer flow through wind turbines and wind farms. *Journal of Wind Engineering and Industrial Aerodynamics*, 99(4), 154–168.  
<https://doi.org/10.1016/j.jweia.2011.01.011>
49. Stevens, R. J. A. M., Graham, J., & Meneveau, C. (2014). A concurrent precursor inflow method for large eddy simulations and applications to finite length wind farms. *Renewable Energy*, 68, 46–50. <https://doi.org/10.1016/j.renene.2014.01.024>
50. Ray PS (1986). *Mesoscale meteorology and forecasting*. American Meteorological Society, Boston, 793 pp ; <https://www.jstor.org/stable/26216020>
51. Porté-Agel, F., Wu, Y.-T., & Chen, C.-H. (2013). A numerical study of the effects of wind direction on turbine wakes and power losses in a large wind farm. *Energies*, 6(10), 5297–5313. <https://doi.org/10.3390/en6105297>
52. Meyers, J., & Meneveau, C. (2010). Large eddy simulations of large wind-turbine arrays in the atmospheric boundary layer. 48th AIAA Aerospace Sciences Meeting Including the New Horizons Forum and Aerospace Exposition. <https://doi.org/10.2514/6.2010-827>
53. Snel, H. (1998). Review of the present status of rotor aerodynamics. *Wind Energy: An International Journal for Progress and Applications in Wind Power Conversion Technology*, 1(S1), 46-69.
54. Burton, T., Jenkins, N., Sharpe, D., & Bossanyi, E. (2011). *Wind energy handbook*. John Wiley & Sons.
55. Herbert, G. J., Iniyar, S., Sreevalsan, E., & Rajapandian, S. (2007). A review of wind energy technologies. *Renewable and sustainable energy Reviews*, 11(6), 1117-1145.
56. Sørensen, J. N. (2011). Aerodynamic aspects of wind energy conversion. *Annual Review of Fluid Mechanics*, 43, 427-448.
57. Vermeer, L. J., Sørensen, J. N., & Crespo, A. (2003). Wind turbine wake aerodynamics. *Progress in aerospace sciences*, 39(6-7), 467-510.
58. Sanderse, B., Van der Pijl, S. P., & Koren, B. (2011). Review of computational fluid dynamics for wind turbine wake aerodynamics. *Wind energy*, 14(7), 799-819.

59. Newman, B. G. (1977). The spacing of wind turbines in large arrays. *Energy conversion*, 16(4), 169-171.,
60. Meneveau, C. (2012). The top-down model of wind farm boundary layers and its applications. *Journal of Turbulence*, (13), N7.
61. Zhou, L., Tian, Y., Baidya Roy, S., Thorncroft, C., Bosart, L. F., & Hu, Y. (2012). Impacts of wind farms on land surface temperature. *Nature Climate Change*, 2(7), 539-543.
62. Stevens, R. J. A. M., & Meneveau, C. (2017). Flow structure and turbulence in wind farms. *Annual Review of Fluid Mechanics*, 49(1), 311–339. <https://doi.org/10.1146/annurev-fluid-010816-060206>
63. International Electrotechnical Commission. IEC 61400-1 Wind energy generation systems - Part 1: Design requirements. <https://webstore.iec.ch/publication/26423>
64. Golston, L., Davies, G., Edwards, R., & Miller, M. (2019). Wind Power: An Energy Technology Distillate from the Andlinger Center for Energy and the Environment at Princeton University. andlinger center . Retrieved April 10, 2023, from [https://www.researchgate.net/profile/Levi-Golston/publication/332401345\\_Wind\\_Power\\_An\\_Energy\\_Technology\\_Distillate/links/5cb1e4a892851c8d22e80b81/Wind-Power-An-Energy-Technology-Distillate.pdf](https://www.researchgate.net/profile/Levi-Golston/publication/332401345_Wind_Power_An_Energy_Technology_Distillate/links/5cb1e4a892851c8d22e80b81/Wind-Power-An-Energy-Technology-Distillate.pdf)
65. Kaimal, J. C., Wyngaard, J. C., Izumi, Y., & Coté, O. R. (1972). Spectral characteristics of surface-layer turbulence. *Quarterly Journal of the Royal Meteorological Society*, 98(417), 563–589. <https://doi.org/10.1002/qj.49709841707>
66. Robertson, A., Sethuraman, L., & Jonkman, J. M. (2018). Assessment of wind parameter sensitivity on extreme and fatigue wind turbine loads. 2018 Wind Energy Symposium. <https://doi.org/10.2514/6.2018-1728>
67. Bachynski, E. E., & Eliassen, L. (2018). The effects of coherent structures on the global response of floating offshore wind turbines. *Wind Energy*, 22(2), 219–238. <https://doi.org/10.1002/we.2280>
68. Doubrawa, P., Churchfield, M. J., Godvik, M., & Simivas, S. (2019). Load response of a floating wind turbine to turbulent atmospheric flow. *Applied Energy*, 242, 1588–1599. <https://doi.org/10.1016/j.apenergy.2019.01.165>
69. Eliassen, L., & Obhrai, C. (2016). Coherence of turbulent wind under neutral wind conditions at Fino1. *Energy Procedia*, 94, 388–398. <https://doi.org/10.1016/j.egypro.2016.09.199>

70. FuE-Zentrum FH Kiel GmbH. FINO1: Forschungsplattformen in Nord- und Ostsee Nr. 1. <https://www.fino1.de/>.
71. Kelley N, Jonkman B. TurbSim - NWTC Information Portal. <https://nwtc.nrel.gov/TurbSim>
72. Simley, E., & Pao, L. Y. (2015). A longitudinal spatial coherence model for wind evolution based on large-eddy simulation. 2015 American Control Conference (ACC). <https://doi.org/10.1109/acc.2015.7171906>
73. Berg, J., Natarajan, A., Mann, J., & Patton, E. G. (2016). Gaussian vs non-Gaussian turbulence: Impact on wind turbine loads. *Wind Energy*, 19(11), 1975–1989. <https://doi.org/10.1002/we.1963>
74. Sathe, A., & Bierbooms, W. (2007). Influence of different wind profiles due to varying atmospheric stability on the fatigue life of wind turbines. *Journal of Physics: Conference Series*, 75, 012056. <https://doi.org/10.1088/1742-6596/75/1/012056>
75. Holtslag, M. C., Bierbooms, W. A., & van Bussel, G. J. (2016). Wind turbine fatigue loads as a function of atmospheric conditions offshore. *Wind Energy*, 19(10), 1917–1932. <https://doi.org/10.1002/we.1959>
76. Churchfield M, Lee S. SOWFA | NWTC Information Portal. <https://nwtc.nrel.gov/SOWFA>
77. Bak, C., Zahle, F., & Bitsche, R. (2013). The DTU 10-MW Reference Wind Turbine. Retrieved April 10, 2023, from [https://orbit.dtu.dk/files/55645274/The\\_DTU\\_10MW\\_Reference\\_Turbine\\_Christian\\_Bak.pdf](https://orbit.dtu.dk/files/55645274/The_DTU_10MW_Reference_Turbine_Christian_Bak.pdf)
78. Hansen, K. S., Barthelmie, R. J., Jensen, L. E., & Sommer, A. (2012). The impact of turbulence intensity and atmospheric stability on power deficits due to wind turbine wakes at Horns Rev wind farm. *Wind Energy*, 15(1), 183-196.
79. Kristoffersen, J. R. (2006). The Horns Rev wind farm and the operational experience with the wind farm main controller. *Revue E-Société Royale Belge des électriciens*, 122(2), 26.

## Appendix A

```
clear all;
close all;
clc
%%

index = 314:366;

for i = 1 : length(index)
    filename{i}= ['I:\Project Bockstigen\data\2000\2nd mean
data\Mean_data',num2str(index(i)),'.mat'];
    filename1{i}= ['I:\Project Bockstigen\data\2000\2nd spectra
data\Spectra',num2str(index(i)),'.mat'];

end

data1=zeros(257,5088);
data2=zeros(1800,5088);
count=1;
count1=0;

%% Anemometers height

z=[9;22;37;40];

%%

for i=1:length(index)

    if index(i)==333| index(i)==334| index(i)==356| index(i)==357| index(i)==338

        data1(:,count:count+95)=NaN;
        data2(:,count:count+95)=NaN;
    else

        %     filename(10:12)=num2str(index(i));
        %     filename1(33:35)=num2str(index(i));
        load(char(filename(i)));
        load(char(filename1(i)));
        data1(:,count:count+95)=Results_S1;
        data2(:,count:count+95)=Results_PSD_fft(1:1800,:);
        count2=1;

        for j=1:24

            %pull out the columns for the mean standard deviation maximum and
            %minimum and put them in separate variables
            mean_var(:,j+count1)=mean_data(:,count2);
            std_var(:,j+count1)=mean_data(:,count2+1);
            max_var(:,j+count1)=mean_data(:,count2+2);
            min_var(:,j+count1)=mean_data(:,count2+3);
```

```

                                % pick out the wind direction and wind speed that is undisturbed by the
mast
                                if mean_data(9,count2)>285 | mean_data(9,count2)<105

                                    wind_speed(1,j+count1)=mean_data(2, count2);
                                    wind_speed(2,j+count1)=mean_data(4, count2);
                                    wind_speed(3,j+count1)=mean_data(6, count2);
                                    wind_speed(4,j+count1)=mean_data(7, count2);
                                    wind_dir(1,j+count1)=mean_data(9, count2);

                                else
                                    wind_speed(1,j+count1)=mean_data(1, count2);
                                    wind_speed(2,j+count1)=mean_data(3, count2);
                                    wind_speed(3,j+count1)=mean_data(5, count2);
                                    wind_speed(4,j+count1)=mean_data(7, count2);
                                    wind_dir(1,j+count1)=mean_data(8, count2);

                                end
                                count2=count2+4;
                            end
                            clear mean_data
                            clear Results_S1
                            clear Results_PSD_fft
                        end
                        count=count+96;
                        count1=count1+24;
                    end

% Find all zero values and make NaN
f=find(mean_var==0);
mean_var(f)=NaN;
min_var(f)=NaN;
max_var(f)=NaN;
std_var(f)=NaN;
clear f
f=find(wind_speed==0);
wind_speed(f)=NaN;
clear f
f=find(wind_dir==0);
wind_dir(f)=NaN;

%plot wind rose
WindRose(wind_dir,wind_speed(3,:))

%plot PDF of wind speed
figure(2)
histogram(wind_speed(3,:), 'Normalization', 'pdf');
xlabel('wind speeds');
ylabel('Frequency');

% calculate mean temperature
temperature=mean_var(10:13,:);
mean_temp=mean(temperature(2:4,:),1,'omitnan');
% calculate potential temperature gradient

```

```

temp_grad=(temperature(4,:)-temperature(2,:))/(25-6);
%calculate velocity gradient squared
vel_grad_sq=((wind_speed(3,:)-wind_speed(2,:))/(37-9)).^2;

% calculate gradient richardson number
Ri_grad=((9.81)./mean_temp).*((temp_grad./vel_grad_sq));

vel_ratio=data1(6,:)./data2(1,:);

%plot PDF of wind speed
f=find(Ri_grad<200); % find values with sensible magnitudes
figure(3)
histogram(Ri_grad(f),'Normalization','pdf');
xlabel('Ri');
ylabel('Frequency');

L=2*size(data2,1);
fs=1;
f = fs*(0:(L/2))/L;

L2=size(data1,1);
df1=0.5/L2;
f1=[df1:df1:0.5];

%Bin average 5-6 M/S
index=find(wind_speed(3,*)>5 & wind_speed(3,*)<6);
day=(index/24);
new_indexes=day*96-1;
avg_5to6_pwelch=mean(data1(:,new_indexes),2,'omitnan');
avg_5to6_FFT=mean(data2(:,new_indexes),2,'omitnan');

figure
loglog(f1,avg_5to6_pwelch,'linewidth',2);
xlabel('frequency (Hz)')
ylabel('Wind spectrum (m^2/Hz)');
grid on;
grid minor
axis tight
hold on
loglog(f(2:L/2),avg_5to6_FFT(2:L/2))
title(['Average PSD for wind speed 5-6 m/s'])
xlabel('frequency (Hz)')
ylabel('Wind spectrum (m^2/Hz)');
legend('Pwelch','FFT')
hold off

clear index
clear new_indexes
%Bin average 6-7 M/S
index=find(wind_speed(3,*)>=6 & wind_speed(3,*)<7);
day=(index/24);
new_indexes=day*96-1;
avg_6to7_pwelch=mean(data1(:,new_indexes),2,'omitnan');

```

```

avg_6to7_FFT=mean(data2(:,new_index),2,'omitnan');

figure
loglog(f1,avg_6to7_pwelch,'linewidth',2);
xlabel('frequency (Hz)')
ylabel('Wind spectrum (m^2/Hz)');
grid on;
grid minor
axis tight
hold on
loglog(f(2:L/2),avg_6to7_FFT(2:L/2))
title(['Average PSD for wind speed 6-7 m/s'])
xlabel('frequency (Hz)')
ylabel('Wind spectrum (m^2/Hz)');
legend('Pwelch','FFT')
hold off

clear index
clear new_index

%Bin average 7-8 M/S
index=find(wind_speed(3,*)>7 & wind_speed(3,*)<8);
day=(index/24);
new_index=day*96-1;
avg_7to8_pwelch=mean(data1(:,new_index),2,'omitnan');
avg_7to8_FFT=mean(data2(:,new_index),2,'omitnan');

figure
loglog(f1,avg_7to8_pwelch,'linewidth',2);
xlabel('frequency (Hz)')
ylabel('Wind spectrum (m^2/Hz)');
grid on;
grid minor
axis tight
hold on
loglog(f(2:L/2),avg_7to8_FFT(2:L/2))
title(['Average PSD for wind speed 7-8 m/s'])
xlabel('frequency (Hz)')
ylabel('Wind spectrum (m^2/Hz)');
legend('Pwelch','FFT')
hold off

clear index
clear new_index

%Bin average 8-9 M/S
index=find(wind_speed(3,*)>8 & wind_speed(3,*)<9);
day=(index/24);
new_index=day*96-1;
avg_8to9_pwelch=mean(data1(:,new_index),2,'omitnan');
avg_8to9_FFT=mean(data2(:,new_index),2,'omitnan');

```



```

figure
loglog(f1,avg_8to9_pwelch,'linewidth',2);
xlabel('frequency (Hz)')
ylabel('Wind spectrum (m^2/Hz)');
grid on;
grid minor
axis tight
hold on
loglog(f(2:L/2),avg_8to9_FFT(2:L/2))
title(['Average PSD for wind speed 8-9 m/s'])
xlabel('frequency (Hz)')
ylabel('Wind spectrum (m^2/Hz)');
legend('Pwelch','FFT')
hold off

clear index
clear new_indexes

%Bin average 09-10 M/S
index=find(wind_speed(3,*)>09 & wind_speed(3,*)<10);
day=(index/24);
new_indexes=day*96-1;
avg_09to10_pwelch=mean(data1(:,new_indexes),2,'omitnan');
avg_09to10_FFT=mean(data2(:,new_indexes),2,'omitnan');

figure
loglog(f1,avg_09to10_pwelch,'linewidth',2);
xlabel('frequency (Hz)')
ylabel('Wind spectrum (m^2/Hz)');
grid on;
grid minor
axis tight
hold on
loglog(f(2:L/2),avg_09to10_FFT(2:L/2))
title(['Average PSD for wind speed 09-10 m/s'])
xlabel('frequency (Hz)')
ylabel('Wind spectrum (m^2/Hz)');
legend('Pwelch','FFT')
hold off

clear index
clear new_indexes

%Bin average 10-11 M/S
index=find(wind_speed(3,*)>10 & wind_speed(3,*)<11);
day=(index/24);
new_indexes=day*96-1;
avg_10to11_pwelch=mean(data1(:,new_indexes),2,'omitnan');
avg_10to11_FFT=mean(data2(:,new_indexes),2,'omitnan');

```

```

figure
loglog(f1,avg_10to11_pwelch,'linewidth',2);
xlabel('frequency (Hz)')
ylabel('Wind spectrum (m^2/Hz)');
grid on;
grid minor
axis tight
hold on
loglog(f(2:L/2),avg_10to11_FFT(2:L/2))
title(['Average PSD for wind speed 10-11 m/s'])
xlabel('frequency (Hz)')
ylabel('Wind spectrum (m^2/Hz)');
legend('Pwelch','FFT')
hold off

clear index
clear new_indexes

%Bin average 11-12 M/S
index=find(wind_speed(3,*)>11 & wind_speed(3,*)<12);
day=(index/24);
new_indexes=day*96-1;
avg_11to12_pwelch=mean(data1(:,new_indexes),2,'omitnan');
avg_11to12_FFT=mean(data2(:,new_indexes),2,'omitnan');

figure
loglog(f1,avg_11to12_pwelch,'linewidth',2);
xlabel('frequency (Hz)')
ylabel('Wind spectrum (m^2/Hz)');
grid on;
grid minor
axis tight
hold on
loglog(f(2:L/2),avg_11to12_FFT(2:L/2))
title(['Average PSD for wind speed 11-12 m/s'])
xlabel('frequency (Hz)')
ylabel('Wind spectrum (m^2/Hz)');
legend('Pwelch','FFT')
hold off

clear index
clear new_indexes

%Bin average 12-13 M/S
index=find(wind_speed(3,*)>12 & wind_speed(3,*)<13);
day=(index/24);
new_indexes=day*96-1;
avg_12to13_pwelch=mean(data1(:,new_indexes),2,'omitnan');
avg_12to13_FFT=mean(data2(:,new_indexes),2,'omitnan');

```

```

figure
loglog(f1,avg_12to13_pwelch,'linewidth',2);
xlabel('frequency (Hz)')
ylabel('Wind spectrum (m^2/Hz)');
grid on;
grid minor
axis tight
hold on
loglog(f(2:L/2),avg_12to13_FFT(2:L/2))
title(['Average PSD for wind speed 12-13 m/s'])
xlabel('frequency (Hz)')
ylabel('Wind spectrum (m^2/Hz)');
legend('Pwelch','FFT')
hold off

clear index
clear new_indexes

%Bin average 13-14 M/S
index=find(wind_speed(3,*)>13 & wind_speed(3,*)<14);
day=(index/24);
new_indexes=day*96-1;
avg_13to14_pwelch=mean(data1(:,new_indexes),2,'omitnan');
avg_13to14_FFT=mean(data2(:,new_indexes),2,'omitnan');

figure
loglog(f1,avg_13to14_pwelch,'linewidth',2);
xlabel('frequency (Hz)')
ylabel('Wind spectrum (m^2/Hz)');
grid on;
grid minor
axis tight
hold on
loglog(f(2:L/2),avg_13to14_FFT(2:L/2))
title(['Average PSD for wind speed 13-14 m/s'])
xlabel('frequency (Hz)')
ylabel('Wind spectrum (m^2/Hz)');
legend('Pwelch','FFT')
hold off

clear index
clear new_indexes

%Bin average 14-15 M/S
index=find(wind_speed(3,*)>14 & wind_speed(3,*)<15);
day=(index/24);
new_indexes=day*96-1;
avg_14to15_pwelch=mean(data1(:,new_indexes),2,'omitnan');
avg_14to15_FFT=mean(data2(:,new_indexes),2,'omitnan');

figure
loglog(f1,avg_14to15_pwelch,'linewidth',2);
xlabel('frequency (Hz)')

```

```
ylabel('Wind spectrum (m^2/Hz)');
grid on;
grid minor
axis tight
hold on
loglog(f(2:L/2),avg_14to15_FFT(2:L/2))
title(['Average PSD for wind speed 14-15 m/s'])
xlabel('frequency (Hz)')
ylabel('Wind spectrum (m^2/Hz)');
legend('Pwelch','FFT')
hold off

clear index
clear new_indexes
```

## Appendix B

### Estimation of the Co-coherence: Main Code

```
clearvars;
close all;
clc;

load('MeanDataAll.mat');

u=MeanWindData_All;

U = nanmean(MeanWindData_All);
z = [9;22;37;40];

% Compute frequency: Here using the same procedure used in the plots
L2=size(MeanWindData_All,1);
df1=0.5/L2;
fs=(df1:df1:0.5);
t=1./fs;

[d,indZ] = getDistance(z);
% indZ is the indice of unique pairs (the upper triangular elements of the distance matrix)
% Get average height and wind speed

meanZ = zeros(size(indZ,1),1);
meanU = zeros(size(indZ,1),1);

for ii=1:size(indZ,1)
    meanZ(ii) = 0.5.*(z(indZ(ii,1))+z(indZ(ii,2)))';
```

```

    meanU(ii) = 0.5.*(U(indZ(ii,1))+U(indZ(ii,2)))';
end
% Estimate the co-coherence
M = round(numel(fs)/20); % 12 blocks
% M = round(numel(t)/20); % 12 blocks

Nm = size(indZ,1);
if mod(M,2)
    cohU = zeros(Nm,round(M/2));
    % = zeros(Nm,round(M/2));
    %cohW = zeros(Nm,round(M/2));
else
    cohU = zeros(Nm,round(M/2)+1);
    %cohV = zeros(Nm,round(M/2)+1);
    %cohW = zeros(Nm,round(M/2)+1);
end
for ii = 1:Nm
    u1 = detrend(u(:,indZ(ii,1)));
    u2 = detrend(u(:,indZ(ii,2)));
    [cohU(ii,:),~,f] = coherence(u1,u2,M,round(M/2),M,1.5); % test
end
maxFreq = 0.15;

guess = [5]; % 1 parameter for the Davenport model
maxFreq = 0.15;
[CoeffFitU,modelFun] =
cohFit(d,f,cohU,guess,meanU,'freqThres',maxFreq,'cohModel','Davenport','z',meanZ);

```

Plot Co-coherence data

```
clf;close all;
figure('position',[200 200 803 903])
t1 = tiledlayout('flow','tilespacing','compact');
for ii=1:Nm
    nexttile
    plot(f,cohU(ii,:),'ko','markerfacecolor',rand(1,3),'markersize',4);hold on;
    %plot(f,modelFun(CoeffFitU,f,d(ii),meanZ(ii),meanU(ii),0),'k')
    txt = ['$z_1 = ',num2str(z(indZ(ii,1))),'$ m, $z_2 = ',num2str(z(indZ(ii,2))),'$ m'];
    label(txt,0.97,0.97,'alignment','right','verticalalignment','top','fontsize',16);
    grid on
    ylim([-0.5,1]);
    %xlim([1/t(end), maxFreq*2])
    xlim([0, 0.5])
    ylim([-0.2, 1.2])
    xlabel('f (Hz)')
    ylabel('\gamma_u')
end
```

### **GetDistance Function**

```
function [d,indZ] = getDistance(z)
% [d,indZ] = getDistance(z) get distance d between two locations and the
% associated indices indZ. This functions can help to speed up the computation
% of the co-coherence of turbulence by avoiding redundant pairs of
% sensors.
%% Author info
% E. Cheynet - UiB - last modified: 25-05-2022
%
% See also coh4Para cpsd pwelch coherence cohere targetCoh getDistance
```

```

Nm = numel(z);
indZ = zeros(Nm,Nm,2);
for ii=1:Nm
    for jj=1:Nm
        indZ(ii,jj,:) = [ii,jj];
    end
end
indZ = reshape(indZ,[],2);
d = triu(abs(z(:)-z(:)'));d = d(:);
k = find(d~=0);
d = d(k);
indZ = indZ(k,:);

end

```

### **coherence Function**

```

function [cocoh, Quad, freq] = coherence(X,Y,WINDOW,NOVERLAP,NFFT,Fs)
% [cocoh, Quad, freq] = coherence(X,Y,WINDOW,NOVERLAP,NFFT,Fs) computes
% the coherence estimate between X and Y.
%
% Author: E Cheynet - University of Stavanger, Norway.
%
% See also cpsd cohere

% get only the fluctuating part
X = detrend(X); % remove mean
Y = detrend(Y); % remove mean

```



```
% get cross spectrum
[pxy, freq] = cpsd(X,Y,WINDOW, NOVERLAP,NFFT,Fs);

% get single point spectrum
pxx = cpsd(X,X,WINDOW, NOVERLAP,NFFT,Fs);
pyy = cpsd(Y,Y,WINDOW, NOVERLAP,NFFT,Fs);

% Normalize the cross spectrum
cocoh = real(pxy./sqrt(pxx.*pyy)); % co-coherence
Quad = imag(pxy./sqrt(pxx.*pyy)); % quad-coherence

end
```